PLOS COMPUTATIONAL BIOLOGY

RESEARCH ARTICLE

Simulation-based Reconstructed Diffusion unveils the effect of aging on protein diffusion in *Escherichia coli*

Luca Mantovanelli[1], Dmitrii S. Linnik[1], Michiel Punter[1], Hildeberto Jardón Kojakhmetov[2], Wojciech M. Śmigiel[1], Bert Poolman[1]*

1 Department of Biochemistry, University of Groningen, Groningen, the Netherlands, **2** Dynamical Systems, Geometry and Mathematical Physics Group, University of Groningen, Groningen, the Netherlands

* b.poolman@rug.nl

Citation: Mantovanelli L, Linnik DS, Punter M, Kojakhmetov HJ, Śmigiel WM, Poolman B (2023) Simulation-based Reconstructed Diffusion unveils the effect of aging on protein diffusion in *Escherichia coli*. PLoS Comput Biol 19(9): e1011093. https://doi.org/10.1371/journal.pcbi.1011093

Editor: Stefan Klumpp, Georg-August-Universitat Gottingen, GERMANY

Received: April 10, 2023

Accepted: August 24, 2023

Published: September 11, 2023

Data Availability Statement: All data are in the manuscript and/or supporting information files.

Funding: The research was funded by the EU Marie-Curie ITN project SynCrop (project number 764591; salary of LM), ERC Advanced grant "ABCVolume" (grant number 670578; salary of WMS) and the NWO National Science Program "The limits to growth" (grant number NWA.1292.19.170; salary of DSL), all grants awarded to BP. The funders had no role in study

Abstract

We have developed Simulation-based Reconstructed Diffusion (SbRD) to determine diffusion coefficients corrected for confinement effects and for the bias introduced by two-dimensional models describing a three-dimensional motion. We validate the method on simulated diffusion data in three-dimensional cell-shaped compartments. We use SbRD, combined with a new cell detection method, to determine the diffusion coefficients of a set of native proteins in *Escherichia coli*. We observe slower diffusion at the cell poles than in the nucleoid region of exponentially growing cells, which is independent of the presence of polysomes. Furthermore, we show that the newly formed pole of dividing cells exhibits a faster diffusion than the old one. We hypothesize that the observed slowdown at the cell poles is caused by the accumulation of aggregated or damaged proteins, and that the effect is asymmetric due to cell aging.

Author summary

Knowledge of the location and mobility of molecules in living cells is paramount to understand cellular processes, protein interactions, folding and function. However, accurately measuring protein mobility in small compartments, such as bacterial cells, is challenging due to various factors. These include the effects of boundaries and compartment geometry, as well as technical limitations like the properties of fluorophores, the diffraction limit of light, and the camera speed. In Escherichia coli cells, the poles are important regions where most of the cellular proteins are synthesized by ribosomes organized in polysomes. At the same time, aggregated or misfolded proteins accumulate at the cell poles, increasing the local macromolecular crowding. We have developed Simulation-based Reconstructed Diffusion to separate the boundary and geometry effects from crowding effects on the observed protein diffusion. Using this method, we investigated how the accumulation of misfolded or damaged proteins at the poles affects the lateral diffusion of various native proteins. We also observed an increase in apparent crowding in the older pole of dividing

design, data collection and analysis, decision to publish, or preparation of the manuscript.

Competing interests: The authors have declared that no competing interests exist.

cells. We related differences in macromolecular crowding in the pole regions of E. coli to aging of the cells, which may impact cellular functions like they do in eukaryotic cells.

Introduction

Diffusion of molecules inside cells plays a crucial role in the functioning of biochemical processes. In prokaryotic cells, which lack membrane-bound compartments, except for the periplasm in Gram-negative bacteria, the majority of cellular processes take place in the cytoplasm. Here, the random motion of (macro)molecules allows for highly sophisticated functions, such as the localization of the septation ring in *Escherichia coli* and the triggering of cell division, which is governed by a reaction-diffusion mechanism [1], the signal transduction that leads to chemotaxis [2], or the translation of mRNA into proteins by polysomes, ribosomes-mRNA assemblies [3].

The cytoplasm of bacteria is an extremely crowded environment, where the concentration of macromolecules, mainly proteins and RNAs, can reach values up to a volume fraction of 15–20% in growing cells [4–6] and even higher in osmotically stressed cells [7–10]. The molecular composition of the cytoplasm is diverse, with molecules spanning in size over more than three orders of magnitudes, from sub-nanometric for ions and metabolites, to micrometric for the chromosome [11,12]. Despite this variation in size and surface properties of the molecules, many cellular components are uniformly distributed throughout the cell [13–15]. Notable exceptions are the chromosome and nucleoid-binding proteins, which localize in the cell center [16,17]; the polysomes, which localize at the poles and cytoplasmic periphery [13,16,18]; and aggregated or misfolded proteins, which localize at the cell poles [19–21] (Fig 1). In addition, there is increasing evidence for the formation of phase-separated liquid droplets or biomolecular condensates in the cytoplasm of microorganisms [22–24], which are metastable structures where certain proteins partition.

Diffusion of spherical particles in aqueous solutions can be described by the Einstein-Stokes equation [25]. However, motion of particles in the highly crowded and inhomogeneous cytoplasm of bacterial cells deviates from the Einstein-Stokes model [14,15,26,27]. We have shown that the apparent diffusion coefficient is solely dependent on the complex mass, that is, the molecular weight of the fluorescently-tagged protein times the oligomeric state [14] (Fig 1). The same conclusion was recently obtained in another study, using a different method [15]. Diffusion of proteins can be influenced by interaction with cell components, provided the interaction strength is high (dissociation constant, K_D, is small) and the mass of the interacting species is large (*e.g.* the cell membrane, the nucleoid, the ribosome or the proteasome complex) [15,28]. The deviation from the Einstein-Stokes equation suggests that protein diffusion depends on the composition and physical state of the cytoplasm. This, in turn, is dependent of (fluidization by) metabolism [29,30], possibly by catalysis-induced enzyme movement [31,32] and environmental stresses [8,33]. Importantly, under given conditions, the macromolecular crowding a protein experiences depends on its own molecular weight, that is, smaller molecules will be less affected by the crowded cytoplasmic environment than bigger ones [14,15,26,27,34] (Fig 1). We have shown that this so-called perceived macromolecular viscosity is not spatially uniform in the cell [14].

Despite the advancements in single molecule fluorescence microscopy [14,15,35–39], diffusion measurements are highly influenced by the effect of confinement, especially in small compartments such as the bacterial cytoplasm [14] and periplasm [40,41], and eukaryotic organelles [42]. Diffusion coefficients near the cell boundaries always appear lower than in the cell center [14,38], which is due to technical and analytical limitations. The time that elapses

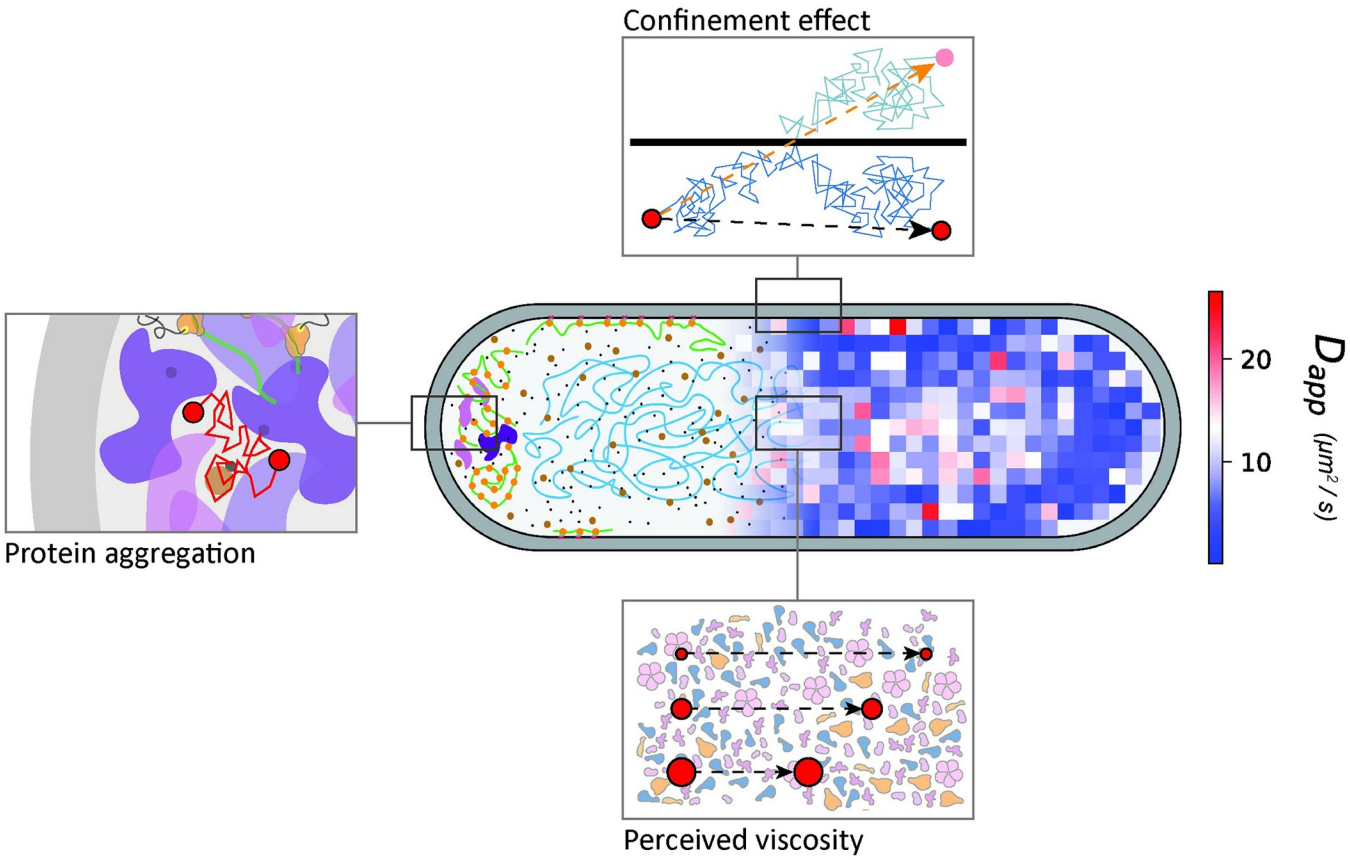

Fig 1. Lateral diffusion in the cytoplasm of *E. coli*. A diffusion map obtained with SMdM is overlayed with a schematic of the cytoplasm of the cell. The top panel highlights the effect of confinement on the measured diffusion, leading to lower diffusion coefficients near the boundaries of the cell. The bottom panel represents the effect of the perceived viscosity by diffusing proteins. Since diffusion scales with the complex mass, bigger particles will be affected more by the crowding of the cytoplasm than smaller molecules and move relatively more slowly, leading to the deviation from the Einstein-Stokes equation. The left panel represents our current hypothesis on the observed slowdown at the cell poles compared to the cell center, with accumulation of aggregated or misfolded proteins impairing the diffusion in these regions.

https://doi.org/10.1371/journal.pcbi.1011093.g001

between two subsequent localization events of a particle in a single molecule experiment is too long to precisely know the particle's trajectory. Therefore, when a particle is diffusing close to a boundary, it is not known whether its trajectory has been affected by the bouncing off the boundary, and so its trajectory is longer than inferred from the localizations. In addition, the diffusion coefficients are obtained from models that do not take the confinement into account. This does not allow to properly separate the effect of confinement from possible physiological slowdown in diffusion of the analyzed species [14] (Fig 1). Moreover, techniques such as Single Particle Tracking (SPT) and Single Molecule displacement Mapping (SMdM) produce a two-dimensional output of a three-dimensional motion, which leads to obvious shortcomings in the estimation of diffusion coefficients of particles moving in the cell cytoplasm.

Some methods to resolve confined diffusion have been developed. Bickel [43] proposed a mathematical solution to obtain the mean square displacement in disks and spheres for particles. Bellotto et al. [15] derived a Ornstein-Uhlenbeck model for fitting of Fluorescence Correlation Spectroscopy (FCS) data acquired in a confined cylinder of infinite length, but they did not consider the geometry of the cell pole regions, where the confinement affects the observed diffusion the most [14]. Finally, diffusion can also be hindered by membraneless structures such as protein aggregates. A study that followed repeated divisions of *E. coli* suggests that cells

that inherit the old pole exhibit a diminished growth rate, decreased offspring production, and an increased incidence of death [44], which is indicative of a locally different composition or structure of the cytoplasm. Asymmetry in the doubling time of old and new pole daughter cells has also been observed in a more recent study in *E. coli* [45]. The underlying mechanisms of aging of bacteria are at best poorly understood.

In this study, we set out to solve the shortcomings of previous methods for analyzing confined diffusion in small compartments, and we apply the new tools to investigate the mobility of proteins in the cytoplasm of *E. coli*. The new method yields diffusion coefficients that are not affected by the effect of confinement or motion along the third dimension. We present a simulation-based analysis, which we named Simulation-based Reconstructed Diffusion (SbRD). We use the method, in combination with a new cell detection tool, to re-analyze a previously acquired dataset [14] and obtain confinement-corrected values for the diffusion of molecules in the *E. coli* cytoplasm. Further, we investigate diffusion near the cell boundaries and at the cell poles to determine how much confinement influences the slowdown in these regions. We test the effect of antibiotics that disrupt the polysome structure in the apparent slowdown of diffusion at the cell poles. Finally, we make observations about asymmetry in diffusion in the bacterial cell, which we associate with aging.

Results

A simulation-based solution to the limitations of confined diffusion

Different mathematical approaches have been attempted to measure the values of diffusion near the boundaries of confined compartments (S1 Text), but they are generally limited by the trajectory of a freely diffusing particle and the model to describing the shape of the compartment [15,43]. We therefore developed a simulation-based approach in which the number of bounces against the surface or the shape of the compartment would not be constraining the outcome. In brief, we developed a method to recursively estimate the diffusion coefficient with an algorithm that makes use of Smoldyn [46] and the SMdM technique [14,35] (Fig 2A). Smoldyn allows the simulation of the motion of particles within a compartment. The compartment can be either mathematically described, or an input of triangulated coordinates of any desired shape. Confinement is accounted for in the motion of the particles, which reflect off the boundaries without losing velocity. We generated diffusion simulations with Smoldyn inside a spherocylinder. As anticipated, the apparent diffusion is underestimated, especially in regions close to the boundaries (S1A, S1E, S3C Figs). The extent of the underestimation is proportional to the diffusion coefficient, and inversely proportional to the size of the confined space and to the acquisition time. Our new algorithm, named Simulation-based Reconstructed Diffusion (SbRD), yields a diffusion coefficient that is homogenous throughout the whole compartment and matches the predefined value used to create the diffusion simulations.

The main steps for the operation of the algorithm are: (i) For simulations, an input diffusion coefficient ($D_{input}{}^{0}$) is used to simulate the diffusion of particles in a spherocylinder, as previously described [14]. For *in vivo* datasets, diffusing particles are measured via stroboscopic illumination microscopy, as previously described. The diffusion map is experimentally obtained by SMdM [14,35]; (ii) The diffusion map yields the total number of displacements per cell and the measured diffusion coefficient ($D_{output}{}^{0}$) for every position; (iii) The starting (x,y) coordinates of all the observed particles are used to place them inside a simulated spherocylinder, and their z coordinates are randomly assigned. This is done by taking a value from a uniform random distribution ranging from the lowest to the highest z value that a particle can have at that specific (x,y) position inside the spherocylinder; (iv) The starting positions (x,y,z) of the particles that belong to a specific pixel of the original diffusion map are selected; (v)

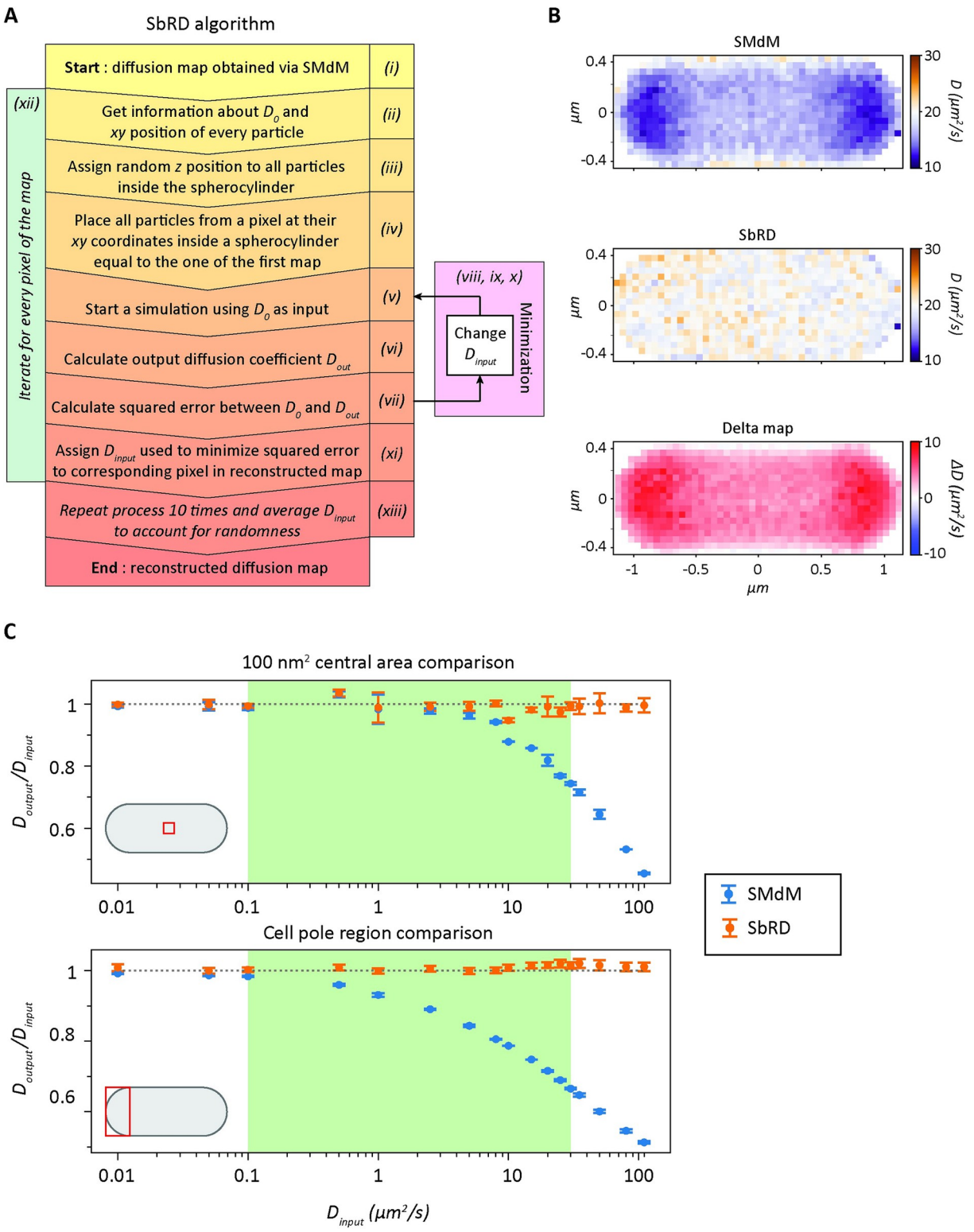

Fig 2. Simulation-based Reconstructed Diffusion. (**A**) Algorithm representation of SbRD. (**B**) Diffusion maps of a spherocylinder obtained by analyzing a Smoldyn simulation created with an input diffusion coefficient of 20 $\mu m^2/s$. Maps are obtained via SMdM analysis (top) and via SbRD (center). The difference between the SbRD map and the SMdM map is depicted in the bottom panel. (**C**) Comparison of the dependence of the ratio of D_{output} / D_{input} in a simulated spherocylinder when analyzing the centermos 100 nm^2 area (top) and the cell pole (bottom) with SMdM and SbRD. The gray dotted line represents the ideal case in which the ratio of D_{output} over D_{input} is one. The relevant range of diffusion coefficients for proteins in the cytoplasm is highlighted in green.

https://doi.org/10.1371/journal.pcbi.1011093.g002

Diffusion simulations are run, using as input diffusion coefficient the D_{output}^{0} value obtained via SMdM; (vi) The diffusion observed by SMdM is analyzed to obtain a new diffusion coefficient for the specific pixel (D_{output}^{1}); (vii) The absolute difference (ε) between D_{output}^{0} and D_{output}^{1} is calculated; (viii) The diffusion simulation process (and subsequent SMdM analysis) is repeated recursively, every time using a different input diffusion coefficient (D_{input}^{i}). (ix) The difference (ε) between D_{output}^{0} and the one obtained through the last simulation (D_{output}^{i+1}) is calculated; (x) The recursion is run until the difference between D_{output}^{N} and D_{output}^{0} reaches a minimum; (xi) The input value (D_{input}^{N-1}) that led to the minimal difference between D_{output}^{N} and D_{output}^{0} is then used to create a new map, which carries D_{input}^{N-1} in the position of the analyzed pixel; (xii) The process is repeated for every pixel, until a map is obtained in which the diffusion coefficients represent the unbiased diffusion values, that is, diffusion coefficients that are corrected for the effect of confinement and for the underestimation caused by a two-dimensional representation of a three-dimensional motion. (xiii) The whole routine is repeated ten times for each cell. The output maps obtained in each iteration are averaged to account for the randomness introduced when assigning the *z* starting position to all particles and for the randomness introduced by Smoldyn in simulating the diffusion of particles [46] (Fig 2A).

Simulation-based Reconstructed Diffusion overcomes limitations of confinement caused by cell boundaries

SbRD together with SMdM allows obtaining more accurate diffusion maps. It is possible to retrieve the actual diffusion coefficient also for the regions close to the cell boundaries (Fig 2B). We also simulated scenarios of a cell displaying slower diffusion at one cell pole, and observed that SbRD is correctly identifying the regions with slower diffusion and faster diffusion coefficients in the cell (S4 Fig).

We then benchmarked SbRD against SMdM data by varying D_{input} from 0.01 to 110 $\mu m^2/s$ and analyzing D_{output} in the innermost 100 nm^2 square of the simulated spherocylinder and in the cell pole region, which are the areas least and most affected by the effect of confinement, respectively. We observe for the innermost region that, as expected, D_{output} obtained via SMdM decreases to 90% of its input value already for D_{input} of 10 $\mu m^2/s$, and that the deviation increases with D_{input} (Fig 2C, top panel). The decrease is more pronounced when the cell pole is analyzed (Fig 2C, bottom panel), with D_{output} obtained via SMdM decreasing to 90% of its input value for D_{input} of 1 $\mu m^2/s$. Importantly, the output of SbRD remains stable throughout the whole set of measurements, with diffusion coefficients near 100% of D_{input} (Fig 2C).

Billiard fitting of rod-shaped bacteria

We acquired single-molecule displacement data from fluorescent images of *E. coli* cells, which we analyzed by SbRD to obtain the diffusion coefficients of a diverse set of fluorescently labelled proteins [14,35]. Briefly, proteins differing in molecular weight and surface charge have been tagged with the photoconvertible fluorescent protein mEos3.2, using 3' gene fusions. mEos3.2 is a green fluorescent protein that can be excited in the range from 450 nm to 530 nm, but the protein can also be photoconverted by a 405 nm fluorescent pulse into a red fluorescent protein with an excitation wavelength maximum of 570 nm. We exploited the photophysics of mEos3.2 to acquire microscopy images of cells expressing the fluorescently tagged protein of interest, using a stroboscopic laser pattern. First, a short low energy 405 nm laser pulse was used to photoconvert on average one protein per cell. Then, two short high-energy 561 nm laser pulses separated by 1.5 ms were used to obtain the initial and final position of the photoconverted protein. The intensity of the 561 nm laser pulses is chosen to photobleach mEos3.2 after the 2^{nd} 561 nm pulse. The sequence of photoactivation, localization and photobleaching of mEos3.2-tagged proteins was

typically repeated a hundred thousand times, allowing to obtain a displacement map of every cell. For a more detailed description we refer to our previous work [14].

The shape of *E. coli* cells is generally assumed to be a spherocylinder [47–51]. Software is available to determine the shape of *E. coli* cells from two-dimensional images [52–54], but estimation and subsequent triangularization of their three-dimensional shape does not necessarily lead to the correct dimension of a cell. For instance, invaginations or protuberances observed on the *xy* plane may not be observed on the *xz* plane. By analyzing our microscopy data, we observed that the vast majority of cells had a shape that could be very well approximated by a two-dimensional projection of a spherocylinder. Therefore, we decided to use this shape for cell detection and modeling, which at the same time allowed for an easy implementation in Smoldyn. To apply SbRD to microscopy data, we developed an algorithm to automatically detect cells as billiards in microscopy images (Fig 3A). Firstly, each field of view was filtered for background noise, yielding clusters of points representing cells. Point clouds were rotated so that their major axis was aligned to the *x*-axis, and subsequently clustered using the equation of a billiard (Eq 1).

$$\begin{cases} (x - cx_{left})^2 + (y - cy)^2 = r^2, \ x < cx_{left} \\ |y - cy| = r, \ cx_{left} \leq x \leq cx_{right} \\ (x - cx_{right})^2 + (y - cy)^2 = r^2, \ x > cx_{right} \end{cases} \quad (1)$$

We refine the cell selections via Maximum Likelihood Estimation using the following assumptions (see Methods –cell clustering and detection): (i) fluorescent points are uniformly distributed throughout the cell; (ii) the cells, here *E. coli*, are modeled as spherocylinders; therefore the 2D projection of their fluorescence (shape of a billiard) appears more populated in the center than near the cell boundary; (iii) all the fluorescent spots observed in a cell have the same probability of being noise; and (iv) every fluorescent point is equally likely to be noise or to be a photoconverted mEos3.2. We then filtered the selected cells for a minimal length of 0.65 μm and a maximal width of 1.5 μm (see methods –cell clustering and detection). If the length of the final billiard describing the shape of the cell was bigger than 3 μm, the algorithm separates the cluster in two billiards, each having half the length of the original one. The refinement step was then repeated for every cluster of two-billiards. This allowed the accurate detection of newly divided cells (Fig 3B), which is often not possible with standard clustering methods, such as Voronoi (Fig 3C). In our previous work [14] we acquired a dataset of diffusing proteins of different complex mass (S1 Table) using SMdM. Here, each cell was clustered using Voronoi clustering. We re-analyzed the full dataset from our previous work with the new clustering method. Importantly, we observe no significant difference between the two datasets, both in the number of detected cells and the diffusion coefficients obtained via SMdM analyses for the cell center (Fig 3D, top) and for the cell poles (Fig 3D, bottom). We then used the information of each cluster to recreate a spherocylinder in Smoldyn [46] having the shape of the corresponding cell, to which we applied the SbRD algorithm (see "A simulation-based solution to the limitation of confined diffusion" from point iii to point xi) to reconstruct diffusion maps, corrected for the confinement effect and bias by 2D models to describe a 3D motion, from the single-molecule fluorescent microscopy data.

SbRD correlates the confinement-corrected diffusion coefficient with the perceived viscosity of the cytoplasm

An advantage of our clustering method is the possibility to precisely identify the cell poles and the cell center by using the radius of the billiard (Fig 3B, bottom), allowing us to analyze these

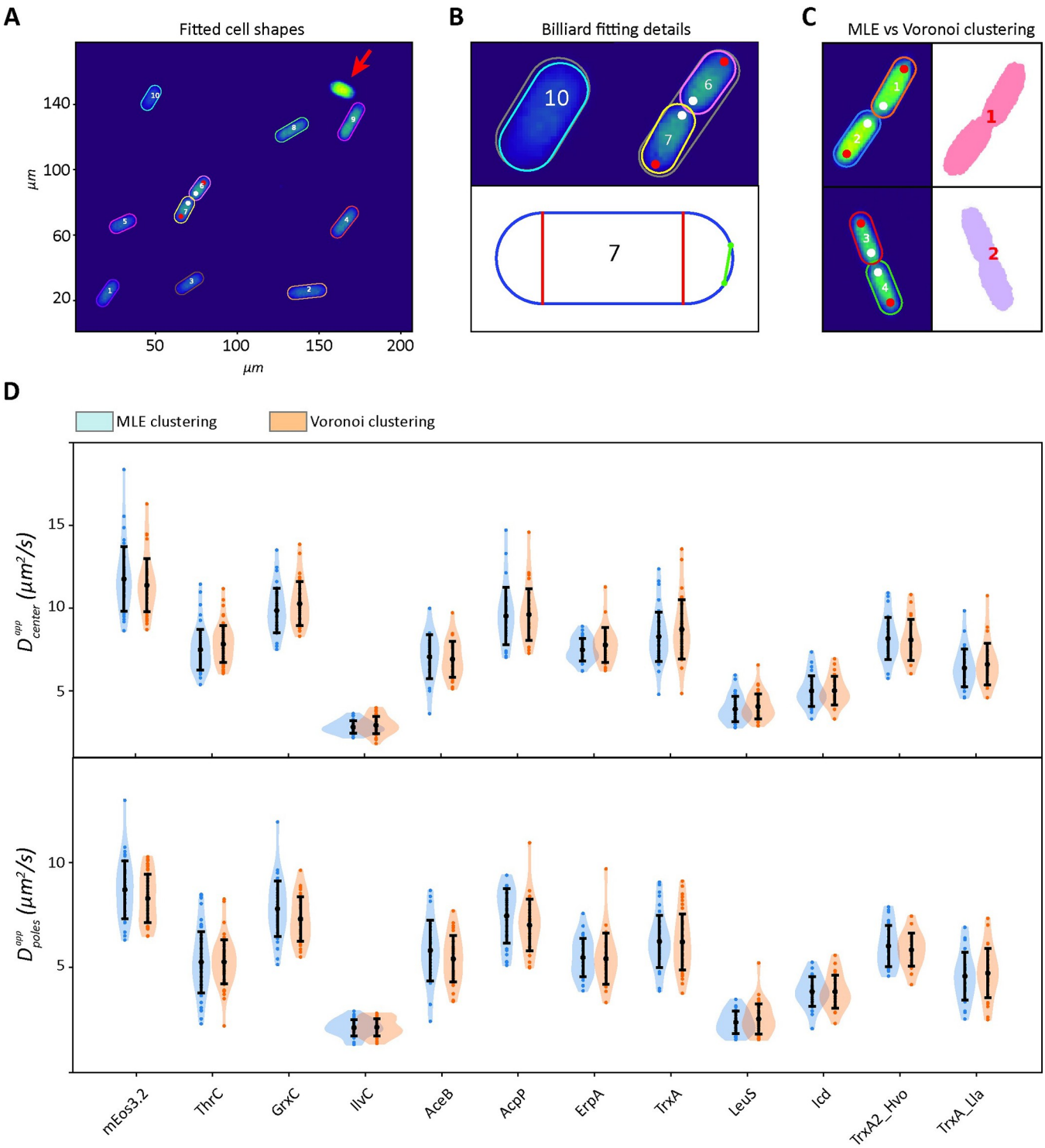

Fig 3. Maximum likelihood-based detection method. (**A**) Field of view and fitting of billiards around the identified cells, using a maximum likelihood estimation method. The cell indicated by a red arrow was discarded because it has too many displacements. (**B**) Details of the fitting process. In the top panel, the initial guess used for fitting, encompassing all the points clustered as a single cell, is represented in grey, while the final fitting is colored. For cells that just completed division, the initial guess encompasses both cells. Due to the abnormal length of the cell, the fitting routine is automatically performed with two billiards to detect both cells. Using the fitting information, it is possible to identify the newly formed cell pole (white dots) and the old one (red dots). The bottom panel shows the billiard used to describe the shape of cell 7. Since cells are represented as billiards, it is possible to obtain accurate estimates of their length and radius, which allow distinguishing the cell poles and cell center for every cell. For cells that just divided and two billiards overlapping, the intersection points are calculated (green dots) and used to draw a line (green line), which is then used to properly model the spherocylinder in the SbRD

routine. (**C**) Comparison of Maximum likelihood method and Voronoi clustering for cell detection. Voronoi clustering cannot properly distinguish cells that are too close to each other. (**D**) Comparison of the apparent diffusion coefficients obtained with SMdM by analyzing the central region (top) and the poles (bottom) of cells identified with Voronoi clustering and with our maximum likelihood method, from images acquired in our previous work [14]. Curves are obtained via kernel density estimation.

https://doi.org/10.1371/journal.pcbi.1011093.g003

regions separately for every cell. We then compared the results obtained via SbRD with the results obtained via SMdM on our previous dataset [14] (S1 Table), and using the new clustering method for cell detection (Table 1, Fig 4). We observe a significant difference in the observed diffusion values for faster diffusing proteins, while for the slower diffusing particles the differences are less or not significant. Notably, we observe a higher statistical significance in the difference between the diffusion coefficient observed at the two cell poles. These results are in line with the observations made via simulations, which indicate that (i) given the fast acquisition time used in SMdM, the effect of confinement on the measured diffusion is less pronounced for slower diffusing particles; and (ii) that the confinement effect is more pronounced in the cell pole regions than in the center of the cell.

We find a correlation between the diffusion coefficient and the complex mass, while we do not observe any correlation between the diffusion coefficient and the number of interactions of the analyzed proteins (S5 Fig). However, since SbRD yields diffusion values corrected for confinement effects, we obtain a new and improved correlation between diffusion and complex mass, with the diffusion coefficient scaling as $D = \alpha M^{-0.6}$. Consequently, the proposed correlation between diffusion and perceived viscosity (η) [14] changes to $\eta = \alpha M_{complex}^{0.27}$ (S5 Fig).

SbRD versus SMdM analysis of the diffusion coefficient at the cell poles

Diffusion measured near the cell boundary and in the cell pole regions of rod-shaped bacteria appears slower than in the cell center due to confinement effects [14,38,55–57]. We recently showed [14] that the ratio between the diffusion coefficient at the cell poles and cell center is lower for SMdM data than for simulated data, where particles are treated as mathematical points that move randomly. This indicates that the slowdown observed in cells must be due to some physiological effect, such as increased crowding in the polar region, possibly due to

Table 1. Lateral diffusion coefficients of cell center and cell poles obtained via SMdM and SbRD for constructs fused to mEos3.2. The columns show the name of the protein, their complex mass, their diffusion values obtained via SMdM (D_{app}) for cell center and cell poles, and the confinement-corrected diffusion values obtained via SbRD (D_{cc}). The Uniprot ID is provided for every protein, except for mEos3.2, for which the Fpbase ID is given.

Protein name	UNIPROT ID	complex mass (kDa)	D_{app}^{center} (μm²/s)		D_{app}^{poles} (μm²/s)		D_{cc}^{center} (μm²/s)		D_{cc}^{poles} (μm²/s)	
			mean	standard deviation	mean	standard deviation	mean	standard deviation	mean	standard deviation
mEos3.2	VUXFR*	25.7	11.8	1.9	8.7	1.4	14.2	2.7	11.6	1.9
ThrC	P00934	72.8	7.5	1.2	5.3	1.5	8.5	1.5	6.4	2.0
GrxC	90AC62	34.8	9.9	1.3	7.8	1.3	11.6	1.7	10.1	2.0
IlvC	P05793	318.9	2.8	0.4	2.1	0.4	3.0	0.4	2.4	0.5
AceB	P08997	85.9	7.0	1.3	5.8	1.4	7.9	1.4	7.2	1.8
AcpP	P0A6A8	34.3	9.5	1.7	7.5	1.3	11.2	2.7	9.6	1.9
ErpA	P0ACC3	75.5	7.5	0.7	5.5	0.9	8.5	1.0	6.7	1.4
TrxA	P0AA25	37.5	8.3	1.5	6.2	1.3	9.4	1.9	7.8	1.8
LeuS	P07813	122.9	3.9	0.8	2.4	0.5	4.2	0.9	2.7	0.7
Icd	P08200	142.8	5.0	0.9	3.8	0.7	5.5	1.1	4.5	0.9
TrxA2_hvo	A0A558GCJ2	37.8	8.2	1.3	6.0	1.0	9.3	1.7	7.4	1.3
TrxA_lla	A0A089XQE8	37.4	6.4	1.1	4.6	1.1	7.2	1.5	5.6	1.6

https://doi.org/10.1371/journal.pcbi.1011093.t001

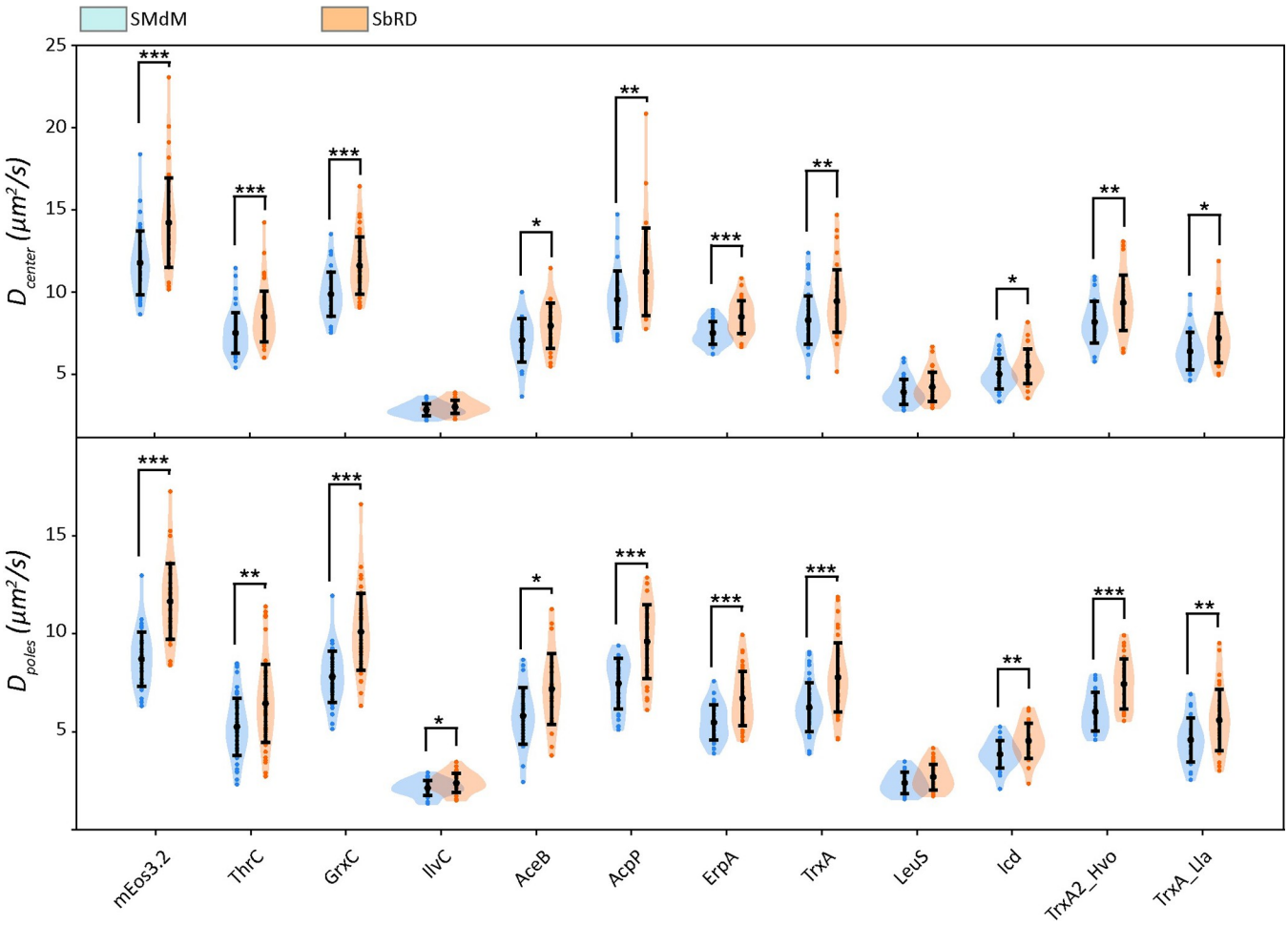

Fig 4. Comparison of the diffusion values obtained via SMdM and via SbRD. Comparison of the apparent diffusion coefficient obtained via SMdM and of the confinement-corrected diffusion coefficient for both the cell center (top) and the cell poles (bottom) for the dataset of proteins tagged with mEos3.2 [14]. Asterisks indicate statistical significance obtained via a Mann-Whitney U test for non-normally distributed data.

https://doi.org/10.1371/journal.pcbi.1011093.g004

aggregation of misfolded or damaged proteins, the presence of the translation machinery, or dynamic structures generating over- and undercrowded regions [14]. One of the key unanswered questions about the diffusion measured at the cell poles is: how much of the observed slowdown is due to confinement and how much is due to physiological effects? It is not possible to decouple these effects by SMdM or other single molecule microscopy techniques. The ratio between the diffusion coefficient at the cell poles and the cell center obtained by SbRD correlates linearly with the ratio obtained by SMdM (S1 Table). This is not observed in simulated cells (Fig 5A). Therefore, the slowdown observed at the poles cannot be attributed solely to the effect of confinement. We compared the ratio between the diffusion at the cell poles and the diffusion at the cell center obtained via SbRD with the one obtained via SMdM for all the analyzed cells clustered as billiards. We observe a D_{pole}/D_{center} ratio of 0.74 ± 0.13 for SMdM and 0.80 ± 0.16 for SbRD (Fig 5B). We analyzed the difference with a Mann-Whitney U rank test for non-normally distributed data and obtained a $p\text{-}value << 0.01$. We therefore conclude that about 20% of the previously observed slowdown at the cell poles can be attributed to confinement effects.

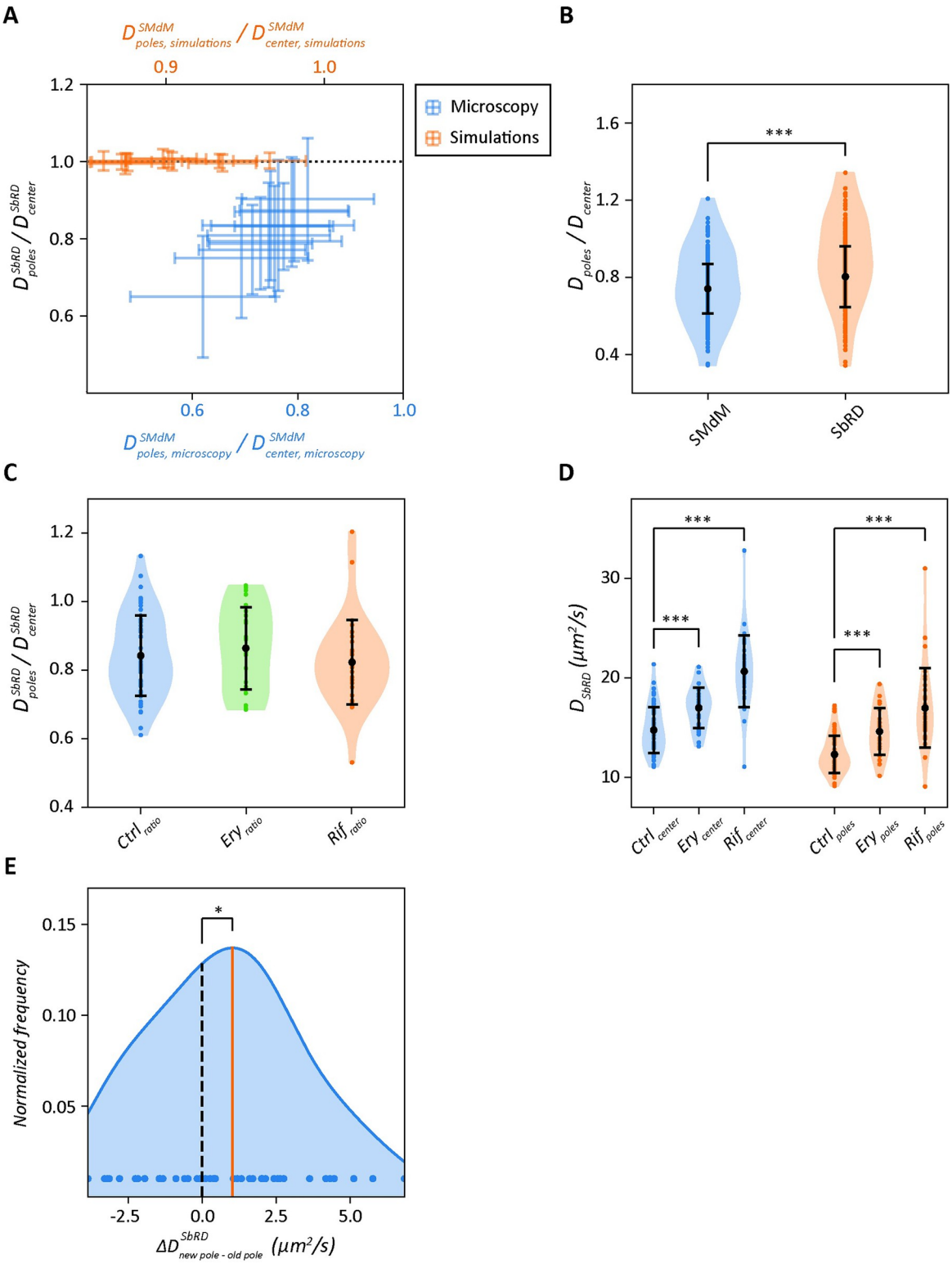

Fig 5. Cell pole analysis of diffusion. (**A**) Comparison of the ratios of the diffusion coefficients at the poles and center of the cell for data analyzed by SbRD and SMdM. The black dotted line shows the case when the diffusion at the poles and center is equal. For simulated data (orange) the ratio obtained with SbRD is equal to 1 for each protein. For microscopy data (blue) we find a positive correlation between the ratio obtained by SMdM and SbRD. (**B**) Ratios of diffusion at the poles and the cell center obtained by SMdM and SbRD. (**C**) Ratios of diffusion at the poles and cell center by SbRD for control cells, and cells treated with 250 μg/ml of erythromycin or 500 μg/ml

rifampicin. (**D**) Diffusion coefficients at the cell center (blue) and poles (orange) for control, erythromycin- and rifampicin-treated cells. (**E**) Distribution of differences in diffusion coefficients between the newly formed cell pole and the old cell pole. The orange line represents the average of the distribution, the black dashed line is the zero. All curves are obtained via kernel density estimation. Statistical significance is indicated with asterisks.

https://doi.org/10.1371/journal.pcbi.1011093.g005

Effect of Rifampicin and Erythromycin on diffusion at the cell poles

The slowdown in diffusion at the cell poles observed via SbRD can be due to: (i) the presence of polysomes, large structures composed of several ribosomes bound to the same mRNA molecule; (ii) clusters of misfolded or damaged proteins that hinder the mobility of other molecules; (iii) or the presence of unknown substructures. To test the first hypothesis, we treated *E. coli* cells expressing mEos3.2 with the antibiotics rifampicin and erythromycin, which disrupt the polysomes via different mode of actions. Rifampicin inhibits DNA-dependent RNA biosynthesis by inhibiting the bacterial RNA-polymerase [58,59], which leads to rapid RNA depletion, particularly of mRNA [60,61], while erythromycin inhibits the assembly of the large ribosomal subunits 50S [62]. Hence, the use of these antibiotics should make the diffusion coefficients at the poles and middle of the cell similar if the polysomes would form a major hindrance for the mobility of mEos3.2. However, we do not observe a significant change in ratio of the diffusion coefficients (Fig 5C), with values of 0.84 ± 0.12, 0.86 ± 0.12 and 0.82 ± 0.12 for untreated cells, cells treated with erythromycin and cells treated with rifampicin, respectively. This is confirmed by the Mann-Whitney U rank test for non-normally distributed data. To further investigate the effect of the antibiotics, we analyzed the absolute values of diffusion. For cells treated with erythromycin, the diffusion at the cell center and at the cell poles show a moderate increase compared to the control sample, while for cells treated with rifampicin the increase is much larger (Fig 5D). For the cell center region we observe diffusion coefficients of 14.76 ± 2.30 $\mu m^2/s$, 16.99 ± 2.04 $\mu m^2/s$ and 20.65 ± 3.61 $\mu m^2/s$, and for the poles 12.31 ± 1.87 $\mu m^2/s$, 14.62 ± 2.35 $\mu m^2/s$ and 16.98 ± 3.99 $\mu m^2/s$ for cells untreated, treated with erythromycin and treated with rifampicin, respectively; the Mann-Whitney U rank confirms these findings ($p\text{-values} << 0.01$). We tentatively conclude that the overall faster diffusion in the presence of the antibiotics is the result of a lower viscosity due to the depletion of mRNA, which is most pronounce upon rifampicin treatment.

Analysis of diffusion at the cell poles indicates asymmetry that correlates with aging

We then analyzed the microscopy data for differences between the cell poles (S6 Fig). We reasoned that differences in aging of the two poles could lead to differences in diffusion, especially because misfolded and aggregated proteins tend to accumulate at the old pole [19–21]. We acquired SMdM data of newly divided cells by selecting fields of view with cells that had just completed the division process (Fig 3B, 3C), and we subsequently applied SbRD to the datasets. We determined the diffusion coefficient corrected for confinement effects of mEos3.2 in each cell individually and find that the diffusion at the old pole is significantly slower than at the new pole. The ratio between the diffusion at the new cell pole and the cell center is 0.86 ± 0.15, while $D_{old\text{-}pole}/D_{center}$ is 0.80 ± 0.13 (S7 Fig). With the assumption that the new cell pole enables on average faster diffusion than the old cell pole, we subtracted $D_{old\text{-}pole}$ from $D_{new\text{-}pole}$ for each cell. We obtained a distribution of residual diffusion coefficients with a mean higher than zero (Fig 5E). We performed a one-sided Wilcoxon signed-rank test to confirm whether the observed difference was significant, and obtained a $p\text{-value} < 0.05$. These findings confirm the hypothesis that aging influences the structure of the cytoplasm at the poles of *E. coli*, causing macromolecules at the older cell pole to diffuse slower than at the new one.

Discussion

We developed a new method to obtain diffusion coefficients that are not affected by confinement effects and bias by 2D modeling of a 3D motion. This method is key not only for measuring lateral diffusion in small compartments, but also for diffusion in proximity of boundaries, such as the plasma or organellar membranes. Despite the enormous advancements offered by SMdM in probing molecule motion compared to other methods, the values obtained near boundaries are affected by the effect of confinement. Our newly developed method SbRD allows examining more precisely regions of the cell that are small and or geometrically more complex.

A method to reconstruct confinement-corrected diffusion coefficients in small cells

The main advantage of the SbRD method is that the shape of the analyzed compartment does not limit the analysis. In fact, compartments of any shape, visualized and reconstructed via triangularization, can be used to recreate an identical virtual compartment. In this way, our method allows reconstructing unbiased diffusion in heterogeneous compartments such as those in eukaryotic cells.

We show by simulations that lateral diffusion measurements performed in small compartments, such as the prokaryotic cell, are bound to underestimate the diffusion coefficient, not only in the regions near the boundary but also in the cell center. The confinement effect in the cell center is mostly due to the 2D observation of a motion in 3D. Using the here developed tool for cell clustering, we precisely detect spatial information such as radius, length, center and orientation angle of a cell. We use this information to reconstruct cells with an assumed spherocylindrical shape in Smoldyn [46]. Recursive diffusion simulations then yield the diffusion coefficient corrected for the confinement effect and the spatial component of motion. This approach led us to (more precisely) estimate the dependence of the diffusion coefficient on the complex mass of the diffusing species and infer from the data the viscosity perceived by a molecule of given molecular mass. We also find that the ratios between the diffusion at the cell poles and the cell center for data acquired via SbRD and via SMdM correlate linearly, as shown in Fig 5A, indicating that the observed slowdown in diffusion at the cell poles can be attributed to physiological effects rather than solely to confinement.

Asymmetric diffusion at the cell poles correlates with aging

We previously obtained indications that the diffusion at the cell poles is slower than in the center of *E. coli* cells [14]. We now determine precisely how much slower the diffusion is at the cell poles, and we show that disassembly of polysomes and depletion of mRNA by antibiotic treatment do not affect the differences in diffusion between the poles and the center of cell. In fact, the diffusion coefficient increases by a similar percentage in each region of the cell, suggesting that the antibiotic treatment has decreased the overall viscosity of the cytoplasm.

Moreover, we were able to precisely detect dividing cells and discriminate new from old cell poles. We show that the poles at the division site exhibit a faster diffusion than the distant poles. The diffusion coefficients at the new and old pole are 86% and 80%, respectively, of the value measured at the cell center. In eukaryotic cells aging is accompanied by an increased cytosolic crowding [63]. Here, we hypothesize that relative slowdown of diffusion at the old pole is consistent with an increase in crowding and an indication of aging in *E. coli*.

Previous studies suggested the possibility of accumulation of aggregated proteins at the cell poles of *E. coli* as a possible cause for the observed aging effects [19]. Łapińska et al. [45],

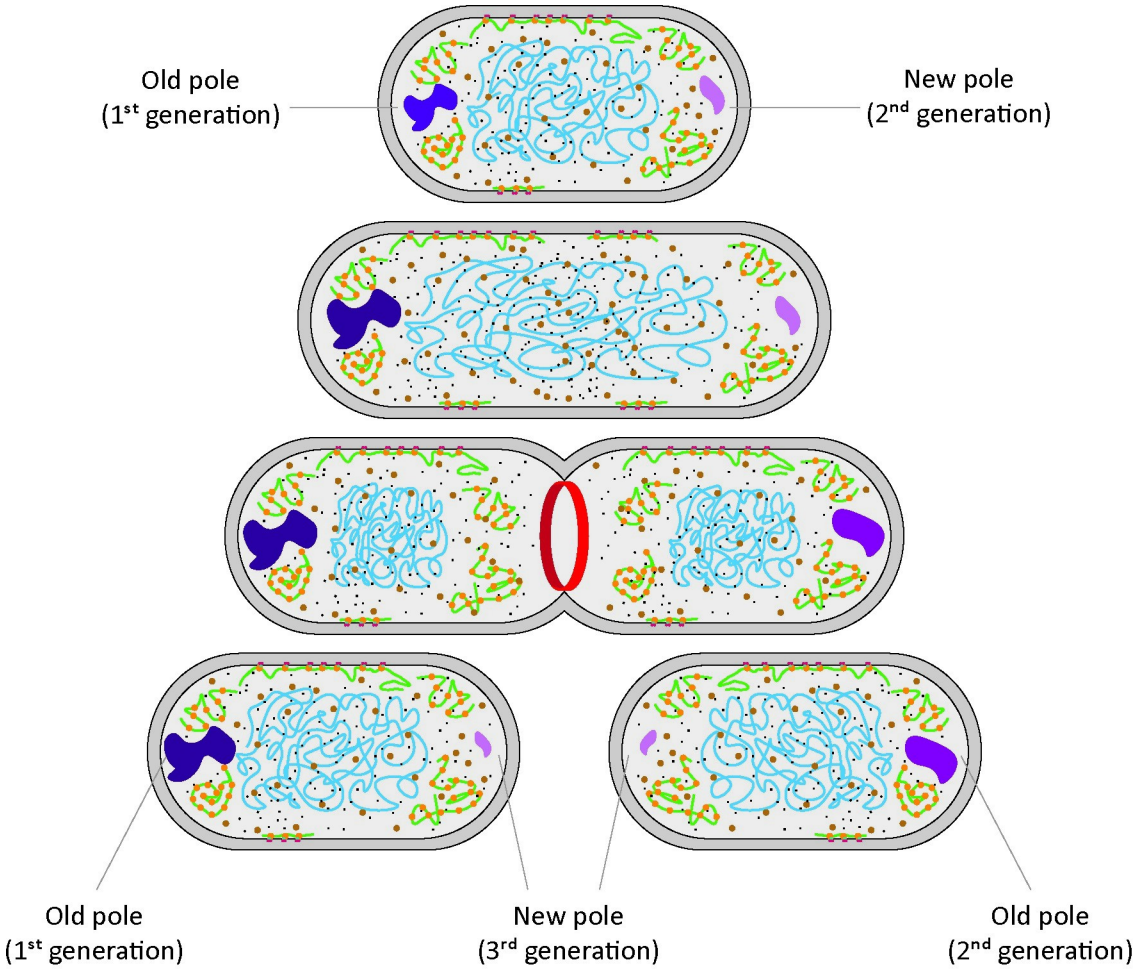

Fig 6. Accumulation of aggregated structures at the cell poles and correlation with aging. A cell with an old pole, with slower diffusion, and a new cell pole, with faster diffusion is shown at the top. As the cell cycle progresses this difference is maintained. When the cell divides and the septation ring forms (red), the two daughter cells will inherit the two cell poles. One of the cells will have the oldest pole as its old pole, while the other will have the new pole of the mother as its old pole.

https://doi.org/10.1371/journal.pcbi.1011093.g006

however, do not observe protein aggregation in the form of inclusion bodies and they argue that proper techniques for the investigation of the structure of cell poles are lacking. We also do not see protein aggregation in the form of inclusion bodies in our dataset but observe a slowdown in the diffusion at the poles. Importantly, we developed a method to more precisely assess the structure of the cytoplasm in the cell pole regions. We conclude that the slower diffusion observed at the old cell pole is an indication of the presence of small clusters of aggregated macromolecules.

The *E. coli* cell cycle is divided in three different phases: the B period, which goes from the cell birth to the beginning of DNA replication; the C period, which goes from the beginning to the termination of DNA replication; and the D period, which represents the time between the termination of DNA replication and cell division [64,65]. During the D period, the two chromosomes segregate to two different parts of the cell, and a period of protein synthesis is necessary for completing the cell division process. If accumulation of static or semi-static structure is a sole characteristic of the cell poles, then the newly formed cell pole should exhibit a diffusion value close to the one measured at the cell center. Since we observe a slower diffusion at the new cell pole (albeit less slow than at the old pole) compared to the one measured at the

cell center, we conclude that the accumulation of damaged or aggregated protein is not a specific characteristic of the cell pole, rather it is a consequence of steric hindrance exerted by the nucleoid, which causes accumulation of structures in nucleoid-free regions of the cell. Based on the currently available literature [19,44,45,66], and on our observations of asymmetry in the diffusion measured at the cell poles of already divided cells, we hypothesize that the observed slowdown is maintained throughout the cell cycle, and that it is possibly passed on from mother cell to daughter cells, where one of the daughter cells will inherit the "slow pole" from the mother, while the other will inherit the "fast pole" (Fig 6).

Concluding remarks

We developed Simulation-based Reconstructed Diffusion (SbRD) to determine diffusion coefficients in diverse compartments, corrected for confinement effects and by the motion of particles along the *z*-axis. We applied the technique to a previously recorded dataset of single-molecule displacements. Using SbRD, we obtain a more precise correlation between the diffusion coefficients and the complex mass of the diffusing species, from which we infer the perceived viscosity for proteins diffusing in the cytoplasm. We recorded new single-molecule displacement datasets to characterize the slower diffusion at the cell poles, and to determine differences in confinement-corrected diffusion at the old and new pole. We correlate slower diffusion at the old poles with aging of the cells. We argue that our new method and analyses tools provide new possibilities for investigating the mechanism of aging of bacteria and other types of cells.

Materials and methods

Live-cell single-molecule microscopy

Media preparation, cell culturing, measurements setup and live-cell imaging was performed as described [14]. Briefly, for each experiment we started a pre-culture of *E. coli*, bearing a pBAD plasmid for the expression of mEos3.2, by scratching a glycerol stock with a sterile inoculation loop and dipping it in a 14-mL plastic culturing tube containing 3 mL of LB medium, prepared following the formula of 10/10/5% (w/v) in MilliQ of NaCl, tryptone (Formedium), and peptone (Formedium), respectively, and supplemented with ampicillin (100 μg/mL). We incubated the pre-culture overnight at 30˚C, with shaking at 200 rpm. On the following day we transferred 30 μL of the LB pre-culture into 3 mL of MOPS-buffered minimal medium (MBM), prepared following the formula in [67], supplemented with 0.1% (v/v) glycerol and ampicillin (100 μg/mL). Cultures were incubated overnight at 30˚C, with shaking at 200 rpm. The next day cells were diluted to a final OD_{600} of 0.05 to 0.08 into prewarmed MBM containing 0.1% (v/v) glycerol, ampicillin (100 μg/mL) and 0.1% (w/v) L-arabinose, and incubated the at 30˚C, with shaking at 200 rpm for 4 to 6 hours before microscopy experiments. Right before the measurements, the cultures were spun down in a tabletop centrifuge and concentrated three times in the growth medium.

To ensure a constant temperature of the microscope during the imaging process, the instrumentation was turned on 4 to 5 hours before the measurement, to minimize the *xy* drift of the samples. Cells were imaged on a clean, non-functionalized high-precision glass slide {specs, manufacturer}, previously sonicated in 5M KOH for 45 minutes and then rinsed 10 times with MilliQ, followed by a drying process via pressurized air. Immobilization of the samples was achieved by depositing 5 μL of concentrated cell suspension on the glass slied and then pressing the cells against the glass surface with solidified agarose pads having the same composition of the MBM medium with a final concentration of agarose of 0.75% (w/v), formed inside a polydimethylsiloxane (PDMS) chamber.

Once the cells settled, we selected an area of our field of view to perform the measurements. We adjusted the focus and the laser beam angle to obtain the highest number of foci, which resulted in the beam angle slightly below that of the critical angle for total internal reflection [highly inclined and laminated optical sheet microscopy [68]]. The camera and the laser were then synchronized in the stroboscopy mode, with illumination pulses necessary to first photoconvert and then detect mEos3.2 every 1.5 ms [14,35]. For a detailed overview of the scripts used for managing the microscope, we refer to our code [69].

Erythromycin treatment was performed for 1 hour after cells reached an OD_{600} of 0.12–0.15 on the day of measurement, by adding erythromycin to the cell culture to a final concentration of 250 ng/μL. Agarose pads were supplemented with the same erythromycin concentration.

Rifampicin treatment was performed as described for erythromycin, using a final concentration of rifampicin of 500 ng/μL. Agarose pads were not supplemented with rifampicin, as this influenced the photoconversion of mEos3.2.

To analyze dividing cells, we visually inspected different fields of view in every sample, and selected areas in which a pair of obviously dividing cells were observed. Dividing cells were then analyzed separately during data analysis.

Cell clustering and detection

The first step in our data analysis pipeline is represented by the detection and clustering of the cells in the imaged field of view. First, the whole analyzed field of view was converted into a 2D histogram in which every bin represents a certain number of fluorescent points. The background value was calculated by taking the median value of the bins. Only the fluorescent points belonging to bins having a value higher than the background value plus one standard deviation were kept and used to create point clouds. For each point cloud the eigenvectors were obtained through the calculation of the covariance matrix, which allowed calculating the angle between the first eigenvector and the *x* axis. From this, an appropriate rotational matrix was applied to the *xy* coordinates of the point cloud, to align its major axis parallel to the *x*-axis. This allowed obtaining a first set of features of the point cloud, namely the length, the width, the rotation angle and the center, which we used to describe a billiard encompassing the point cloud. Shape refinement was obtained by fitting an improved billiard around the point cloud via maximum likelihood estimation. The fitting was performed with the following assumptions: (i) the fluorescent molecules are uniformly distributed throughout the cells. Since the cells are spherocylinders imaged in two dimensions, the number of molecules observed is directly proportional to the thickness of the cells; therefore the boundary areas are less populated than the center; (ii) every observed point is equally likely as any other to be due to random noise; (iii) the probability of a point being random noise is equal to the probability of a point being a fluorescent molecule. From these three assumptions we obtain the following probability mass function for each particle (Eq 2):

$$p_i(x,y) = \left(\frac{h_i(x,y)}{V(X,Y)} + \frac{1}{N(X,Y)}\right)/2 \tag{2}$$

Where N is the number of particles (X,Y) inside the spherocylinder, V is the volume of the spherocylinder, which is modeled based on all the points (X,Y) within the spherocylinder, and $h_{x,y}$ is the thickness of the spherocylinder at the xy coordinate of the detected point. All these parameters depend on the size of the spherocylinder, which is described by its length, its radius, its center and its rotation angle. Therefore, these are used as fitting parameters to identify the best spherocylinder describing the detected point cloud.

The identified cells are then filtered based on their shape, discarding cells that are shorter than 0.65 μm (possibly cells that are partially out of the field of view), or wider than 1.5 μm (possibly noise or drift). Cells having a length bigger than 3 μm were automatically reanalyzed as dividing cells. In case of overlapping billiards for dividing cells, the intersection points were identified by calculating the intersection of the two semicircles describing the two adjacent cell poles. From this, it was possible to calculate the volume of the two spherical sections of the neighboring cell poles. Since any of the observed points could belong to either cell, the final volume used to calculate the probability density had to be adjusted by adding the intersection volume (Eq 3):

$$p_i(x,y) = \left(\frac{h_{i,1}(x,y) + h_{i,2}(x,y)}{V(X_1,Y_1) + V(X_2,Y_2) + V(X_{int},Y_{int})} + \frac{1}{N(X,Y)} \right) /2 \quad (3)$$

Where N is the number of particles (X,Y) inside the two spherocylinders, $V(X_1,Y_1)$ is the volume of the first spherocylinder, $V(X_2,Y_2)$ is the volume of the second spherocylinder, $V(X_{int},Y_{int})$ is the volume of the intersection between the two spherocylinders, h_1 is the thickness of the first spherocylinder at the xy coordinate of the detected point, and h_2 is the thickness of the second spherocylinder at the xy coordinate of the detected point.

Finally, the identified cells are visually inspected and discarded if not suitable for analysis (e.g. dividing cells not correctly identified, for which the total length is shorter than 3 μm). The fitted spherocylinders are then used to create clusters from the point clouds. The data analysis is then performed on each cluster separately, ignoring the points that are not included in the cluster. More information on the cell detection and clustering can be found on our code [69].

SMdM analysis

SMdM analysis was performed as described previously [14], with the exception that cell clustering was performed prior to peak pairing. Briefly, we recorded several consecutive movies for each field of view and paired the observed localizations from the two consecutive frames of the stroboscopic illumination pattern. For single-molecule analysis, we used the STORM-analysis package developed by the Zhuang laboratory, which is included in the 3D-DAOSTORM program for peak detection [70]. After a full movie was analyzed, the localizations were corrected for xy drift.

All the detected peaks in each field of view were used for clustering and for finding the shape of the spherocylinder that best describes the shape of the cell, as reported in the section above.

Displacements were obtained from all the peaks belonging to a single cell, by pairing localizations from the two consecutive frames of the stroboscopic illumination pattern. We set a maximum distance of 600 nm between any two peaks to be paired: the distance is then used to find all possible peak pairs for each couple of frames. To obtain a displacement, we match each peak in the first frame of the couple with all the peaks falling within a radius of 600 nm in the second frame. This procedure is repeated for all frame couples of each field of view. A hard filter based on the number of detected displacements was then applied, discarding cells with less than 2000 or more than 20000 displacements, as described [14].

A pixel map with pixel size of 100 nm^2 was obtained for each cell, with every pixel containing the information of all the peak pairs for which the starting position is located inside the pixel itself. Each pixel of the map containing a minimum number of displacements (set to 10 in our study) was then fitted using a modified two-dimensional probability density function (PDF), which accounts for a linear background effect k, which can be caused by an ambiguity

in the assignment of peak pairs [14] (Eq 4):

$$p(r,t) = \frac{1}{1 - e^{-\frac{r_{max}^2}{4Dt}} + \frac{k}{2} r_{max}^2} \left(\frac{2r}{4Dt} e^{-\frac{r^2}{4Dt}} + kr \right) \quad (4)$$

Since t is known, as it represents the time between two stroboscopic laser pulses, the PDF was fitted on the detected displacements r, using the diffusion coefficient D and the background value k as fitting parameters. Displacements were detected using the MLE clustering method (see section above) for SbRD. Displacements were detected both using the MLE clustering method and Voronoi clustering when comparing the two clustering methods using SMdM.

Given our advanced cell detection method, we could perform an accurate identification of the different cell regions, namely the cell poles and the cell center. Fitting a billiard to detect the shape of the cells allows obtaining precise information about their length and their radius, which in turn allow identifying the cell pole regions and the central region of the cell. All the displacements belonging to the same region were then used to perform the fitting using Eq 10, yielding information about the diffusion coefficient in the different regions of the cell [14].

The dependence of the diffusion coefficient on the complex mass was fitted using a power law relationship $D = \alpha M_{complex}^{\beta}$, where $M_{complex}$ is the complex mass and α and β are fitting parameters [14]. Fitting was performed using the function *curve_fit* included in the SciPy library [71].

Smoldyn simulations

Simulations were performed using the software Smoldyn [46], as described [14]. A diffusion coefficient and a time-step length are used as input for the simulations, together with the total simulation time. At every time step, Smoldyn randomly selects a step length from a normal distribution having as mean the squared mean squared displacement calculated from the input diffusion coefficient, as well as a random direction in the *xyz* space for each particle. These values are used to simulate the motion of every particle in the system at every time step, until the total simulation time is reached. In our simulations we used a time step of 0.1 ms and a total simulation time of 2 seconds. Particles every 15 steps (1.5 ms) were then paired together in displacements, the results were benchmarked against the microscopy data.

We used Smoldyn to generate two separate datasets. First, we simulated the motion of particles using input diffusion coefficients ranging from 0.01 to 110 $\mu m^2/s$ in a spherocylinder having length and width of 2.25 and 0.9 μm, respectively, as these reflect the average cell size observed in our previous work [14]. We then generated a second dataset using input diffusion coefficients ranging from 1 to 20 $\mu m^2/s$ in a spherocylinder with a length ranging from 1.4 to 2.9 μm and width ranging from 0.6 to 1.5 μm, always keeping the ratio between length and width higher than 2 and lower than 4 to reproduce actual dimensions of *E. coli*.

We analyzed the output of our simulation using the same approach adopted for SMdM measurements and compared the results with those obtained by SbRD (see section *SbRD analysis*). The equation used for simulated data does not account for linear background correction (Eq 5):

$$p(r,t) = \frac{2r}{4Dt} e^{-\frac{r^2}{4Dt}} \quad (5)$$

More information about the simulations can be found on our code [69].

SbRD analysis

Simulation-based Reconstructed Diffusion (SbRD) was applied by using Smoldyn simulations on SMdM analyses. A collection of points representing a cell, either coming from a Smoldyn simulation or from a microscopy experiment, is analyzed using SMdM (see section *SMdM analysis*). This analysis provides a pixel map of the cell, in which for each pixel the diffusion coefficient, as well as the *xy* start and end positions of each displacement, are known. For microscopy measurements, the new cell clustering method allowed us to determine the length and radius of the spherocylinder in which the diffusing particles are confined, which could be modeled in Smoldyn. In the case of dividing cells, the septum is modeled as a reflecting wall passing through the intersection points of the two billiards, encompassing two separate cells, and parallel to the *z* axis. In the case of data from Smoldyn simulations, the length and radius of the spherocylinder are known. This information was then used to start a recursive simulation in Smoldyn by placing a number of particles equal to the number of displacements in their respective *xy* starting position inside the pixel, with the *z* position randomly assigned to each particle inside the spherocylinder, which in the case of microscopy data was modeled as described in *Cell clustering and detection*. A simulation lasting for 1.5 ms, with simulation steps of 0.1 ms is started, using as input diffusion coefficient the value of the pixel obtained via SMdM (see section *Smoldyn simulations*). The output of this simulation is then used to perform a fitting using equation 12, with *D* as fitting parameter. The squared difference between the output diffusion obtained via simulations and the diffusion obtained via SMdM is then calculated. The program then recursively iterates the simulation process until such squared difference reaches a minimum. We utilize a gradient descent method that is included in the *minimize* method of the *Scipy* [71] library as minimization procedure. The input diffusion coefficient used to obtain the output diffusion coefficient that minimizes the squared difference is then regarded as the real diffusion coefficient of the pixel. This process is then repeated 10 times for each pixel to account for the randomness introduced by Smoldyn [46] in the choice of the step length and the direction of motion, as well as for the randomness introduced in the placing the particle along the *z*-axis. The process is then repeated for every pixel of the original SMdM map, from which an SbRD map is obtained. The pixel-by-pixel differences between the SbRD map and the SMdM map are used to construct a difference map. More information about the SbRD analysis can be found on our code [69].

Statistical analysis

All statistical analyses were performed using the Python package *stats* from the SciPy library [71]. Shapiro-Wilk test for normality [72] was used to check whether the data are normally distributed, using a level of confidence of 5%. The test assumes the null hypothesis for data that are normally distributed. Therefore, if the obtained *p-value* is lower than 0.05 the null hypothesis is rejected and the data are assumed to be non-normally distributed. Non-normally distributed datasets are visualized via kernel density estimation.

The Mann-Whitney U rank test [73] was used to test whether the means of two non-normally distributed datasets are equal. In the case of comparing means of datasets, *i.e.* when no prior assumptions are made and no precise outcome is expected, such as in the case of comparing the diffusion coefficients of cells treated with antibiotics, a two sided test was performed. In the case of comparing means of datasets in which a specific outcome was expected, such as in the case of comparing the diffusion coefficient of the two different cell poles, a one-sided test was performed.

The Wilcoxon signed-rank test [74] was used to test whether the median of a dataset coming from paired measurements is significantly different from zero. This test was used to assess

whether the difference in diffusion between the new cell pole and the old cell pole was significantly higher than zero, therefore it was conducted as a one sided test. Statistical significance in pictures are indicated with 1 asterisk (*) for *p-value* < 0.05, 2 asterisks (**) for *p-value* < 0.01 and 3 asterisks (***) for *p-value* < 0.001.

Supporting information

S1 Text. A mathematical solution to confined diffusion: Exploration of a folding approach to solve confined diffusion mathematically and overview of its limitations.
(PDF)

S2 Text. Diffusion on a closed interval: Mathematical demonstration of Eq 3 from S1 Text.
(PDF)

S1 Algorithm. General algorithm used to estimate the diffusion coefficient from the billiard approach. We assume that the coordinate system is located at the center of the billiard.
(PDF)

S1 Fig. Mathematical solution to confinement. (**A**) Effect of confinement on diffusion. Diffusion simulations performed in a billiard at different input diffusion coefficients. The position of the particles was measured every 1.5 ms. The higher the diffusion coefficient used for the simulation, the more pronounced the confinement effect is. (**B**). Sketch of the (random) motion of a particle in a 1 dimensional closed interval. The point x_0 stands for the initial position of the particle at t = 0. The point x(t) represents the position of the particle at time $t > 0$. In this scenario, and for fixed $t > 0$, there are several possibilities for measuring a particle's position at x(t). The first scenario is that the particle travels to its measured position without bouncing. Another scenario is that the particle arrives at its measured position after bouncing (on the boundaries) once. In this way, there are infinitely many ways in which the particle can reach its measured position, depending on the number of bounces the particle made. However, the probability of each case is inversely proportional to the total distance traveled (Eq 3, Supporting Information–Diffusion on a closed interval). In B we show the distances traveled for 0 and 1 bounce (against each boundary). (**C**) Solutions of the diffusion equation on a bounded interval with length L = 2 μm, D = 2 $\mu m^2/s$, and t = {0.05, 0.1, 0.5} seconds, shown in blue, red, and purple respectively. The solid lines correspond to the analytical solution [3], while the dashed curves correspond to [5]. From top to bottom we show comparisons for 0, 1, and 2 bounces. Notice that, in this example, accounting for two bounces already gives a sufficiently good approximation of the analytical solution (bottom panel). (**D**) A few trajectories of a billiard in the Bunimovich stadium. We show one 0-bounce (solid line) and four 1-bounce billiard trajectories (dashed lines). The bouncing points (x_{c1}, y_{c1}) and (x_{c2}, y_{c2}) are solutions of the system of equations shown under [7]. (**E**) Diffusion maps of a billiard obtained by analyzing a Smoldyn simulation created with an input diffusion coefficient of 20 $\mu m^2/s$, with particles' position measured every 1.5 ms. Maps are obtained via SMdM analysis (left) and via mathematical method analysis (right). The difference between the mathematical map and the SMdM map is depicted in the bottom panel.
(TIF)

S2 Fig. Two-dimensional diffusion in confined space with bouncing. (**A**) Example of a rectangular billiard. We show all possible billiard trajectories that take the particle from $p_0 = (x_0, y_0)$ to $pf = (x_1, y_1)$ after 0 (solid line) and 1 bounce (dashed lines), and we show one trajectory with 2 bounces (dash-dot lines). The solution of the diffusion equation in this scenario can be computed by adding all the "boundary-less" densities accounting for the different lengths of

the billiard trajectories that take the particle from p0 to pf. (**B**) Comparison of the density ρ for a square of sides 2, with D = 2, ρ(x, y, 0) = δ2(x, y), and Neumann boundary conditions. In all figures the blue surface corresponds to the analytical solution, the green surface indicates the density without accounting for any bounce, and the red surface shows the density accounting for one bounce. Left for t = 0.01, center for t = 0.1, and right for t = 0.25. Notice that, as expected, the more bounces, the better the approximation.
(TIF)

S3 Fig. Limitation of the mathematical model for confined diffusion. (A) Schematic of Penrose unilluminable room. A ray (vector) starting from the center of the room can never reach the regions colored in yellow, regardless of the number of bounces against the perimeter. A particle moving by random motion (dashed line) can reach any region in the room. (B) Limitations of using a 2D model to describe a 3D motion. Left panel: the motion of a particle moving in 3D space (blue arrow) is projected on a 2D surface (orange arrow). The observed distance is shorter than the actual travelled distance, leading to an underestimation of the diffusion coefficient. Right panel: the effect of the overestimation of the billiard perimeter. By observing the projection of a 3D spherocylinder in 2D, we use as billiard's perimeter its largest xy projection. When displacements are binned in a pixel close to the boundaries, the bouncing of particles will likely occur against a different section of the spherocylinder, where the circumference of the billiard is smaller. In this way, the calculated bouncing path (orange arrow) overestimates the actual path (blue arrow), leading to an overestimation of the diffusion coefficient near the boundaries. (C) Diffusion maps of a spherocylinder obtained by analyzing a Smoldyn simulation created with an input diffusion coefficient of 20 μm2/s. Maps are obtained via SMdM analysis (left) and via mathematical method analysis (right). The difference between the mathematical map and the SMdM map is depicted in the bottom panel.
(TIF)

S4 Fig. SbRD applied to simulated multiple-component diffusion. We simulated multiple component diffusion in a spherocylinder (using Smoldyn) with an input diffusion coefficient of 20 $\mu m^2/s$ for the first component. The second component was simulated with different dynamics. (**A**) Aggregation is simulated by defining a spherical region in the cell pole with input diffusion coefficient of 2 $\mu m^2/s$. Particles diffusing outside of the aggregation region could not enter the sphere, and vice versa particles confined in the aggregation region could not diffuse outside of the sphere (**B**) Interaction with a cellular component located at the cell pole is simulated by defining a spherical region in the cell pole, in which particles change their diffusion coefficient from 20 $\mu m^2/s$ to 16 $\mu m^2/s$ upon entering the region and retrieve their original diffusion coefficient (20 $\mu m^2/s$) after exiting the region. (**C**) Diffusion of two different species is simulated by defining a spherical region at the cell pole in which a species diffuses with D is 10 $\mu m^2/s$, while the other species freely diffuse in the whole spherocylinder, including the spherical region, with a diffusion coefficient of 20 $\mu m^2/s$. SbRD allows in all cases to retrieve information about the genuine diffusion coefficient in the cell and near the boundaries, without masking the effect of aggregation, interaction or multiple diffusing species. An advanced method using SbRD together with recursive recognition of slower or faster diffusing regions could allow detecting anomalies in cells.
(TIF)

S5 Fig. Correlation of Diffusion and perceived viscosity with the Complex Mass as revealed by SbRD. (**A**) Dependence of the Dcenter measured with SbRD on the complex mass of a set of cytoplasmic proteins [14] (S1 Table). Native proteins are indicated in blue, mEos3.2 is indicated in red. The gray trendline is obtained by calculating the dependence of the diffusion

coefficient on the complex mass. (**B**) Intracellular perceived viscosity as a function of the molecular weight of protein complexes. The trendline is obtained by fitting the formula $\eta = \alpha M^{0.27}$, obtained by the difference between the Einstein-Stokes equation and our model for the relationship between diffusion and complex mass [14].
(TIF)

S6 Fig. Difference in diffusion between fast and slow cell poles. A previously acquired dataset [14] was re-analyzed with SbRD. The ratios between the diffusion values obtained at the cell poles and at the cell center were labeled as faster pole and slower pole for each cell. All faster poles were clustered together, and their value was compared with the clustered slower poles. The faster cell pole cluster has a value of 0.89 ± 0.17, while the slower cell pole cluster has a value of 0.72 ± 0.17. The difference in values between the two clusters is significant, with a p-value $<< 0.01$, calculated from a Mann-Whitney U rank test for non-normally distributed samples.
(TIF)

S7 Fig. Difference in diffusion between old and new cell pole. The acquired dataset of dividing cells was analyzed with SbRD. The presented data are averages of the whole dataset. The average of the ratios between the diffusion at the old cell pole and the diffusion at the cell center was compared with the average of the ratios between the diffusion at the new cell pole and at the diffusion at the cell center. The old cell pole cluster has a value of 0.80 ± 0.13, while the new cell pole cluster has a value of 0.86 ± 0.15. The difference in values between the two clusters is significant, with a p-value < 0.05, calculated from a Mann-Whitney U rank test for non-normally distributed samples.
(TIF)

S1 Table. Dataset from (14). The cell numbers represent single, non-dividing cells without visible aggregation of the expressed protein. The columns show the target protein, number of analyzed cells, abundance, loneliness, molecular weight, oligomeric state (1—monomer, 2—homodimer, 4—homotetramer), and complex mass. The complex mass is the sum of the molecular weight of the monomeric protein plus mEos3.2 and multiplied by the oligomeric state number. The mean and SD of D_{app} center are shown in the last two columns. The UniProt ID is reported for all proteins, except for mEos3.2, for which the Fpbase ID is given.
(PDF)

Author Contributions

Conceptualization: Luca Mantovanelli, Bert Poolman.

Data curation: Luca Mantovanelli, Michiel Punter.

Formal analysis: Luca Mantovanelli, Hildeberto Jardón Kojakhmetov.

Funding acquisition: Bert Poolman.

Investigation: Luca Mantovanelli, Dmitrii S. Linnik, Wojciech M. Śmigiel.

Methodology: Luca Mantovanelli, Hildeberto Jardón Kojakhmetov.

Project administration: Luca Mantovanelli, Bert Poolman.

Resources: Bert Poolman.

Software: Luca Mantovanelli, Michiel Punter.

Supervision: Luca Mantovanelli, Bert Poolman.

Validation: Luca Mantovanelli, Dmitrii S. Linnik.

Visualization: Luca Mantovanelli.

Writing – original draft: Luca Mantovanelli, Bert Poolman.

Writing – review & editing: Luca Mantovanelli, Bert Poolman.

References

1. Pavin N, Paljetak HČ, Krstić V. Min-protein oscillations in Escherichia coli with spontaneous formation of two-stranded filaments in a three-dimensional stochastic reaction-diffusion model. Phys Rev E. 2006 Feb 13; 73(2):021904.
2. Lipkow K, Andrews SS, Bray D. Simulated Diffusion of Phosphorylated CheY through the Cytoplasm of Escherichia coli. Journal of Bacteriology. 2005 Jan; 187(1):45–53. https://doi.org/10.1128/JB.187.1.45-53.2005 PMID: 15601687
3. Bakshi S, Siryaporn A, Goulian M, Weisshaar JC. Superresolution imaging of ribosomes and RNA polymerase in live Escherichia coli cells. Molecular Microbiology. 2012 Jul 1; 85(1):21–38. https://doi.org/10.1111/j.1365-2958.2012.08081.x PMID: 22624875
4. Cayley S, Lewis BA, Guttman HJ, Record MT. Characterization of the cytoplasm of Escherichia coli K-12 as a function of external osmolarity: Implications for protein-DNA interactions in vivo. Journal of Molecular Biology. 1991 Nov 20; 222(2):281–300.
5. Zimmerman SB, Trach SO. Estimation of macromolecule concentrations and excluded volume effects for the cytoplasm of Escherichia coli. Journal of Molecular Biology. 1991 Dec 5; 222(3):599–620. https://doi.org/10.1016/0022-2836(91)90499-v PMID: 1748995
6. Spitzer J, Poolman B. How crowded is the prokaryotic cytoplasm? FEBS Letters. 2013; 587(14):2094–8. https://doi.org/10.1016/j.febslet.2013.05.051 PMID: 23735698
7. Mika JT, Poolman B. Macromolecule diffusion and confinement in prokaryotic cells. Current Opinion in Biotechnology. 2011 Feb 1; 22(1):117–26. https://doi.org/10.1016/j.copbio.2010.09.009 PMID: 20952181
8. Mika JT, Bogaart GVD, Veenhoff L, Krasnikov V, Poolman B. Molecular sieving properties of the cytoplasm of Escherichia coli and consequences of osmotic stress. Molecular Microbiology. 2010; 77(1):200–7. https://doi.org/10.1111/j.1365-2958.2010.07201.x PMID: 20487282
9. van den Berg J, Boersma AJ, Poolman B. Microorganisms maintain crowding homeostasis. Nat Rev Microbiol. 2017 May; 15(5):309–18. https://doi.org/10.1038/nrmicro.2017.17 PMID: 28344349
10. Liu B, Hasrat Z, Poolman B, Boersma AJ. Decreased Effective Macromolecular Crowding in Escherichia coli Adapted to Hyperosmotic Stress. Journal of Bacteriology. 2019 Apr 24; 201(10):e00708–18. https://doi.org/10.1128/JB.00708-18 PMID: 30833357
11. Schmidt A, Kochanowski K, Vedelaar S, Ahrné E, Volkmer B, Callipo L, et al. The quantitative and condition-dependent Escherichia coli proteome. Nat Biotechnol. 2016 Jan; 34(1):104–10. https://doi.org/10.1038/nbt.3418 PMID: 26641532
12. Mori M, Zhang Z, Banaei-Esfahani A, Lalanne JB, Okano H, Ludwig C. From coarse to fine: the absolute Escherichia coli proteome under diverse growth conditions. Molecular Systems Biology. 2021 May 1; 17(5):e9536. https://doi.org/10.15252/msb.20209536 PMID: 34032011
13. Dersch S, Rotter DAO, Graumann PL. Heterogeneity of Subcellular Diffusion in Bacteria Based on Spatial Segregation of Ribosomes and Nucleoids. MIP. 2022; 32(5–6):177–86. https://doi.org/10.1159/000526846 PMID: 36070705
14. Śmigiel WM, Mantovanelli L, Linnik DS, Punter M, Silberberg J, Xiang L, et al. Protein diffusion in Escherichia coli cytoplasm scales with the mass of the complexes and is location dependent. Science Advances. 2022 Aug 12;8(32):eabo5387.
15. Bellotto N, Agudo-Canalejo J, Colin R, Golestanian R, Malengo G, Sourjik V. Dependence of diffusion in Escherichia coli cytoplasm on protein size, environmental conditions, and cell growth. Amir A, Barkai N, Mullineaux CW, editors. eLife. 2022 Dec 5; 11:e82654. https://doi.org/10.7554/eLife.82654 PMID: 36468683
16. Chai Q, Singh B, Peisker K, Metzendorf N, Ge X, Dasgupta S, et al. Organization of Ribosomes and Nucleoids in Escherichia coli Cells during Growth and in Quiescence. J Biol Chem. 2014 Apr 18; 289(16):11342–52. https://doi.org/10.1074/jbc.M114.557348 PMID: 24599955
17. Wu F, Swain P, Kuijpers L, Zheng X, Felter K, Guurink M, et al. Cell Boundary Confinement Sets the Size and Position of the E. coli Chromosome. Current Biology. 2019 Jul 8; 29(13):2131–2144.e4.

18. Bakshi S, Choi H, Weisshaar JC. The spatial biology of transcription and translation in rapidly growing Escherichia coli. Frontiers in Microbiology [Internet]. 2015 [cited 2022 Jan 26];6. Available from: https://www.frontiersin.org/article/10.3389/fmicb.2015.00636 PMID: 26191045

19. Winkler J, Seybert A, König L, Pruggnaller S, Haselmann U, Sourjik V, et al. Quantitative and spatio-temporal features of protein aggregation in Escherichia coli and consequences on protein quality control and cellular ageing. The EMBO Journal. 2010 Mar 3; 29(5):910–23. https://doi.org/10.1038/emboj.2009.412 PMID: 20094032

20. Coquel AS, Jacob JP, Primet M, Demarez A, Dimiccoli M, Julou T, et al. Localization of Protein Aggregation in Escherichia coli Is Governed by Diffusion and Nucleoid Macromolecular Crowding Effect. PLOS Computational Biology. 2013 Apr 25; 9(4):e1003038. https://doi.org/10.1371/journal.pcbi.1003038 PMID: 23633942

21. Schramm FD, Schroeder K, Jonas K. Protein aggregation in bacteria. FEMS Microbiology Reviews. 2020 Jan 1; 44(1):54–72. https://doi.org/10.1093/femsre/fuz026 PMID: 31633151

22. Babl L, Giacomelli G, Ramm B, Gelmroth AK, Bramkamp M, Schwille P. CTP-controlled liquid–liquid phase separation of ParB. Journal of Molecular Biology. 2022 Jan 30; 434(2):167401. https://doi.org/10.1016/j.jmb.2021.167401 PMID: 34902429

23. Guilhas B, Walter JC, Rech J, David G, Walliser NO, Palmeri J, et al. ATP-Driven Separation of Liquid Phase Condensates in Bacteria. Molecular Cell. 2020 Jul 16; 79(2):293–303.e4. https://doi.org/10.1016/j.molcel.2020.06.034 PMID: 32679076

24. Jin X, Lee JE, Schaefer C, Luo X, Wollman AJM, Payne-Dwyer AL, et al. Membraneless organelles formed by liquid-liquid phase separation increase bacterial fitness. Science Advances [Internet]. 2021 Oct [cited 2022 Jan 26]; Available from: https://www.science.org/doi/abs/10.1126/sciadv.abh2929 PMID: 34669478

25. Einstein A. Zur Theorie der Brownschen Bewegung. Annalen der Physik. 1906; 324(2):371–81.

26. Kumar M, Mommer MS, Sourjik V. Mobility of cytoplasmic, membrane, and DNA-binding proteins in Escherichia coli. Biophys J. 2010 Feb 17; 98(4):552–9. https://doi.org/10.1016/j.bpj.2009.11.002 PMID: 20159151

27. Nenninger A, Mastroianni G, Mullineaux CW. Size Dependence of Protein Diffusion in the Cytoplasm of Escherichia coli. Journal of Bacteriology [Internet]. 2010 Sep [cited 2022 Jan 26]; Available from: https://journals.asm.org/doi/abs/10.1128/JB.00284-10 PMID: 20581203

28. Schavemaker PE, Śmigiel WM, Poolman B. Ribosome surface properties may impose limits on the nature of the cytoplasmic proteome. Sourjik V, editor. eLife. 2017 Nov 20; 6:e30084.

29. Parry BR, Surovtsev IV, Cabeen MT, O'Hern CS, Dufresne ER, Jacobs-Wagner C. The Bacterial Cytoplasm Has Glass-like Properties and Is Fluidized by Metabolic Activity. Cell. 2014 Jan 16; 156(1):183–94. https://doi.org/10.1016/j.cell.2013.11.028 PMID: 24361104

30. Joyner RP, Tang JH, Helenius J, Dultz E, Brune C, Holt LJ, et al. A glucose-starvation response regulates the diffusion of macromolecules. Singer RH, editor. eLife. 2016 Mar 22; 5:e09376.

31. Ramm B, Goychuk A, Khmelinskaia A, Blumhardt P, Eto H, Ganzinger KA, et al. A diffusiophoretic mechanism for ATP-driven transport without motor proteins. Nat Phys. 2021 Jul; 17(7):850–8.

32. Golestanian R, Liverpool TB, Ajdari A. Propulsion of a Molecular Machine by Asymmetric Distribution of Reaction Products. Phys Rev Lett. 2005 Jun 10; 94(22):220801. https://doi.org/10.1103/PhysRevLett.94.220801 PMID: 16090376

33. Dix JA, Verkman AS. Crowding Effects on Diffusion in Solutions and Cells. Annual Review of Biophysics. 2008; 37(1):247–63. https://doi.org/10.1146/annurev.biophys.37.032807.125824 PMID: 18573081

34. Klumpp S, Scott M, Pedersen S, Hwa T. Molecular crowding limits translation and cell growth. Proceedings of the National Academy of Sciences. 2013 Oct 15; 110(42):16754–9. https://doi.org/10.1073/pnas.1310377110 PMID: 24082144

35. Xiang L, Chen K, Yan R, Li W, Xu K. Single-molecule displacement mapping unveils nanoscale heterogeneities in intracellular diffusivity. Nat Methods. 2020 May; 17(5):524–30. https://doi.org/10.1038/s41592-020-0793-0 PMID: 32203387

36. Tran BM, Linnik DS, Punter CM, Śmigiel WM, Mantovanelli L, Iyer A, et al. Super-resolving microscopy reveals the localizations and movement dynamics of stressosome proteins in Listeria monocytogenes. Commun Biol. 2023 Jan 14; 6(1):1–15.

37. Huang B, Bates M, Zhuang X. Super-Resolution Fluorescence Microscopy. Annu Rev Biochem. 2009 Jun 1; 78(1):993–1016. https://doi.org/10.1146/annurev.biochem.77.061906.092014 PMID: 19489737

38. English BP, Hauryliuk V, Sanamrad A, Tankov S, Dekker NH, Elf J. Single-molecule investigations of the stringent response machinery in living bacterial cells. PNAS. 2011 Aug 2; 108(31):E365–73. https://doi.org/10.1073/pnas.1102255108 PMID: 21730169

39. Mantovanelli L, Gaastra BF, Poolman B. Chapter One—Fluorescence-based sensing of the bioenergetic and physicochemical status of the cell. In: Model MA, Levitan I, editors. Current Topics in Membranes [Internet]. Academic Press; 2021 [cited 2022 Jan 26]. p. 1–54. (New Methods and Sensors for Membrane and Cell Volume Research; vol. 88). Available from: https://www.sciencedirect.com/science/article/pii/S106358232100017X

40. Brass JM, Higgins CF, Foley M, Rugman PA, Birmingham J, Garland PB. Lateral diffusion of proteins in the periplasm of Escherichia coli. Journal of Bacteriology. 1986 Mar; 165(3):787–95. https://doi.org/10.1128/jb.165.3.787-795.1986 PMID: 3005237

41. Sochacki KA, Shkel IA, Record MT, Weisshaar JC. Protein Diffusion in the Periplasm of E. coli under Osmotic Stress. Biophysical Journal. 2011 Jan 5; 100(1):22–31. https://doi.org/10.1016/j.bpj.2010.11.044 PMID: 21190653

42. Partikian A, Ölveczky B, Swaminathan R, Li Y, Verkman AS. Rapid Diffusion of Green Fluorescent Protein in the Mitochondrial Matrix. J Cell Biol. 1998 Feb 23; 140(4):821–9. https://doi.org/10.1083/jcb.140.4.821 PMID: 9472034

43. Bickel T. A note on confined diffusion. Physica A: Statistical Mechanics and its Applications. 2007 Apr 1; 377(1):24–32.

44. Stewart EJ, Madden R, Paul G, Taddei F. Aging and Death in an Organism That Reproduces by Morphologically Symmetric Division. PLOS Biology. 2005 Feb 1; 3(2):e45. https://doi.org/10.1371/journal.pbio.0030045 PMID: 15685293

45. Łapińska U, Glover G, Capilla-Lasheras P, Young AJ, Pagliara S. Bacterial ageing in the absence of external stressors. Philosophical Transactions of the Royal Society B: Biological Sciences. 2019 Oct 7; 374(1786):20180442. https://doi.org/10.1098/rstb.2018.0442 PMID: 31587633

46. Andrews SS. Smoldyn: particle-based simulation with rule-based modeling, improved molecular interaction and a library interface. Bioinformatics. 2017 Mar 1; 33(5):710–7. https://doi.org/10.1093/bioinformatics/btw700 PMID: 28365760

47. Zhu Y, Mohapatra S, Weisshaar JC. Rigidification of the Escherichia coli cytoplasm by the human antimicrobial peptide LL-37 revealed by superresolution fluorescence microscopy. Proceedings of the National Academy of Sciences. 2019 Jan 15; 116(3):1017–26. https://doi.org/10.1073/pnas.1814924116 PMID: 30598442

48. Mohapatra S, Weisshaar JC. Functional mapping of the E. coli translational machinery using single-molecule tracking. Molecular Microbiology. 2018; 110(2):262–82. https://doi.org/10.1111/mmi.14103 PMID: 30107639

49. Peters VFD, Vis M, Tuinier R, Lekkerkerker HNW. Phase separation in mixed suspensions of bacteria and nonadsorbing polymers. J Chem Phys. 2021 Apr 21; 154(15):151101. https://doi.org/10.1063/5.0045435 PMID: 33887938

50. Zhu Y, Mustafi M, Weisshaar JC. Biophysical Properties of Escherichia coli Cytoplasm in Stationary Phase by Superresolution Fluorescence Microscopy. mBio. 2020 Jun 16; 11(3):e00143–20. https://doi.org/10.1128/mBio.00143-20 PMID: 32546611

51. Gameiro D, Pérez-Pérez M, Pérez-Rodríguez G, Monteiro G, Azevedo NF, Lourenço A. Computational resources and strategies to construct single-molecule metabolic models of microbial cells. Briefings in Bioinformatics. 2016 Sep 1; 17(5):863–76. https://doi.org/10.1093/bib/bbv096 PMID: 26515531

52. Smit JH, Li Y, Warszawik EM, Herrmann A, Cordes T. ColiCoords: A Python package for the analysis of bacterial fluorescence microscopy data. PLOS ONE. 2019 Jun 19; 14(6):e0217524. https://doi.org/10.1371/journal.pone.0217524 PMID: 31216308

53. Paintdakhi A, Parry B, Campos M, Irnov I, Elf J, Surovtsev I, et al. Oufti: an integrated software package for high-accuracy, high-throughput quantitative microscopy analysis. Molecular Microbiology. 2016; 99(4):767–77. https://doi.org/10.1111/mmi.13264 PMID: 26538279

54. Ducret A, Quardokus EM, Brun YV. MicrobeJ, a tool for high throughput bacterial cell detection and quantitative analysis. Nat Microbiol. 2016 Jun 20; 1(7):1–7. https://doi.org/10.1038/nmicrobiol.2016.77 PMID: 27572972

55. Bohrer CH, Xiao J. Complex Diffusion in Bacteria. In: Duménil G, van Teeffelen S, editors. Physical Microbiology [Internet]. Cham: Springer International Publishing; 2020 [cited 2023 Jan 31]. p. 15–43. (Advances in Experimental Medicine and Biology). Available from: https://doi.org/10.1007/978-3-030-46886-6_2

56. Mortensen KI, Flyvbjerg H, Pedersen JN. Confined Brownian Motion Tracked With Motion Blur: Estimating Diffusion Coefficient and Size of Confining Space. Frontiers in Physics [Internet]. 2021 [cited 2023 Jan 31];8. Available from: https://www.frontiersin.org/articles/10.3389/fphy.2020.583202

57. Rowland DJ, Tuson HH, Biteen JS. Resolving Fast, Confined Diffusion in Bacteria with Image Correlation Spectroscopy. Biophysical Journal. 2016 May 24; 110(10):2241–51. https://doi.org/10.1016/j.bpj.2016.04.023 PMID: 27224489

58. Campbell EA, Korzheva N, Mustaev A, Murakami K, Nair S, Goldfarb A, et al. Structural Mechanism for Rifampicin Inhibition of Bacterial RNA Polymerase. Cell. 2001 Mar 23; 104(6):901–12. https://doi.org/10.1016/s0092-8674(01)00286-0 PMID: 11290327

59. Mosaei H, Zenkin N. Inhibition of RNA Polymerase by Rifampicin and Rifamycin-Like Molecules. EcoSal Plus [Internet]. 2020 Apr 27 [cited 2023 Feb 3];9(1). Available from: https://journals.asm.org/doi/10.1128/ecosalplus.ESP-0017-2019

60. Chen H, Shiroguchi K, Ge H, Xie XS. Genome-wide study of mRNA degradation and transcript elongation in Escherichia coli. Molecular Systems Biology. 2015 Jan; 11(1):781. https://doi.org/10.15252/msb.20145794 PMID: 25583150

61. Hamouche L, Poljak L, Carpousis AJ. Ribosomal RNA degradation induced by the bacterial RNA polymerase inhibitor rifampicin. RNA. 2021 Aug 1; 27(8):946–58. https://doi.org/10.1261/rna.078776.121 PMID: 34099575

62. Usary J, Champney WS. Erythromycin inhibition of 50S ribosomal subunit formation in Escherichia coli cells. Molecular Microbiology. 2001; 40(4):951–62. https://doi.org/10.1046/j.1365-2958.2001.02438.x PMID: 11401702

63. Liu B, Mavrova SN, van den Berg J, Kristensen SK, Mantovanelli L, Veenhoff LM, et al. Influence of Fluorescent Protein Maturation on FRET Measurements in Living Cells. ACS Sens. 2018 Sep 28; 3(9):1735–42. https://doi.org/10.1021/acssensors.8b00473 PMID: 30168711

64. Donachie WD. The Cell Cycle of Escherichia Coli. Annual Review of Microbiology. 1993; 47(1):199–230. https://doi.org/10.1146/annurev.mi.47.100193.001215 PMID: 8257098

65. Wallden M, Fange D, Lundius EG, Baltekin Ö, Elf J. The Synchronization of Replication and Division Cycles in Individual E. coli Cells. Cell. 2016 Jul 28; 166(3):729–39.

66. Lindner AB, Madden R, Demarez A, Stewart EJ, Taddei F. Asymmetric segregation of protein aggregates is associated with cellular aging and rejuvenation. Proceedings of the National Academy of Sciences. 2008 Feb 26; 105(8):3076–81. https://doi.org/10.1073/pnas.0708931105 PMID: 18287048

67. Neidhardt FC, Bloch PL, Smith DF. Culture Medium for Enterobacteria. Journal of Bacteriology [Internet]. 1974 Sep [cited 2022 Jan 26]; Available from: https://journals.asm.org/doi/abs/10.1128/jb.119.3.736-747.1974 PMID: 4604283

68. Tokunaga M, Imamoto N, Sakata-Sogawa K. Highly inclined thin illumination enables clear single-molecule imaging in cells. Nat Methods. 2008 Feb; 5(2):159–61. https://doi.org/10.1038/nmeth1171 PMID: 18176568

69. MembraneEnzymology. MembraneEnzymology/SbRD: SbRD analysis for Escherichia coli cytoplasm v0.1 [Internet]. Zenodo; 2023 [cited 2023 Feb 4]. Available from: https://zenodo.org/record/7605250

70. Babcock H, Sigal YM, Zhuang X. A high-density 3D localization algorithm for stochastic optical reconstruction microscopy. Optical Nanoscopy. 2012 Jul 16; 1(1):6. https://doi.org/10.1186/2192-2853-1-6 PMID: 25431749

71. Virtanen P, Gommers R, Oliphant TE, Haberland M, Reddy T, Cournapeau D, et al. SciPy 1.0: fundamental algorithms for scientific computing in Python. Nat Methods. 2020 Mar; 17(3):261–72. https://doi.org/10.1038/s41592-019-0686-2 PMID: 32015543

72. Shapiro SS, Wilk MB. An Analysis of Variance Test for Normality (Complete Samples). Biometrika. 1965; 52(3/4):591–611.

73. McKnight PE, Najab J. Mann-Whitney U Test. In: The Corsini Encyclopedia of Psychology [Internet]. John Wiley & Sons, Ltd; 2010 [cited 2022 Jan 26]. p. 1–1. Available from: https://onlinelibrary.wiley.com/doi/abs/10.1002/9780470479216.corpsy0524

74. Kim HY. Statistical notes for clinical researchers: Nonparametric statistical methods: 1. Nonparametric methods for comparing two groups. Restorative Dentistry & Endodontics. 2014 Aug 1; 39(3):235–9. https://doi.org/10.5395/rde.2014.39.3.235 PMID: 25110650